A Multiphase Godunov Method for Compressible Multifluid and Multiphase Flows

Richard Saurel* and Rémi Abgrall†

*_IUSTI, CNRS UMR 6595, 5 rue Enrico Fermi, 13453 Marseille Cedex 13, France; and_
†_Université de Bordeaux I, 351 cours de la Libération, 33405 Talence, France_
E-mail: richard@iusti.univ-mrs.fr and abgrall@math.u-bordeaux.fr

We propose a new model and a solution method for two-phase compressible flows. The model involves six equations obtained from conservation principles applied to each phase, completed by a seventh equation for the evolution of the volume fraction. This equation is necessary to close the overall system. The model is valid for fluid mixtures, as well as for pure fluids. The system of partial differential equations is hyperbolic. Hyperbolicity is obtained because each phase is considered to be compressible. Two difficulties arise for the solution: one of the equations is written in non-conservative form; non-conservative terms exist in the momentum and energy equations. We propose robust and accurate discretisation of these terms. The method solves the same system at each mesh point with the same algorithm. It allows the simulation of interface problems between pure fluids as well as multiphase mixtures. Several test cases where fluids have compressible behavior are shown as well as some other test problems where one of the phases is incompressible. The method provides reliable results, is able to compute strong shock waves, and deals with complex equations of state. © 1999 Academic Press

Key Words: multiphase flows; hyperbolic models; interfaces; Godunov methods; non-conservative equations; shock waves; Eulerian methods.

1. INTRODUCTION

Compressible multifluid flows occur in many situations in which fluids have different physical or thermodynamic properties and are separated by interfaces. A classical example is an interface between air and helium under shock wave. Other well-known examples are the Richtmyer–Meshkov instabilities between two gases and the behavior of a gas bubble in a liquid under shock wave. Many numerical simulations of such processes are based on the Euler or Navier–Stokes equations augmented by one or several species of conservation equations in order to build reasonable equation of state parameters at the interface. Indeed, all

classical numerical methods produce artificial diffusion of contact discontinuities, resulting in artificial fluid mixing at the interface. In this artificial mixture, pressure and temperature computations are inaccurate with this approach. When the fluid properties are close (low density variations and low parameters of the equation of state changes), the classical methods induce low deviations. But in many circumstances, the fluid parameters are very different, as are the densities from one fluid to another. Consider, for example, an interface separating a liquid and a gas, or as in many applications with detonations, an interface between a gas and a solid. Under such conditions, methods based on the Euler equations augmented by species conservation equations are ill-adapted. These methods fail at the second time step. Abgrall [1], Karni [26], and Abgrall [2] showed that even when the fluid properties are close, standard algorithms based upon species conservation equations induce large errors in the pressure and velocity computation.

Often, the equations of state found in the literature have only a limited range of validity (especially for solids and liquids). When the thermodynamic parameters provided by a numerical method are slightly outside this domain of validity, the pressure, entropy, sound speed, etc., that are computed have no physical meaning (negative pressure, etc.). In many cases, an interface is the physical location where the flow parameters are close to the limits of validity of the equation of state. Hence a careful and clean treatment of interfaces is mandatory. In a previous paper, we detailed how to circumvent these problems for fluids governed by the Stiffened gas equation of state (EOS) (Harlow and Amsden [24], Godunov *et al.* [19]) with interfaces between them. Our objective was, and is still, to solve in each space location the same equations with the same numerical methods. Of course, it is possible to solve the same equations everywhere with different numerical schemes, as done, for example, with front tracking methods (see, for example, Cocchi and Saurel [8]). A discussion of the various alternatives for solving multifluid flows is given in Saurel and Abgrall [40]. Our opinion is that it is much simpler and more efficient to solve the same equations with the same numerical method. A way to do this in the simplified situation of fluids under hydrodynamic regime, governed by the Stiffened gas EOS, was proposed in Saurel and Abgrall [40], but this method was restricted to fluids governed by the Stiffened gas equation of state only. Also, the way to include other physical effects such as mass transfer at the interface was unclear. This is why we now propose another model, relying on two-phase flow equations. Two-phase flow equations allow determination of the thermodynamic and kinematic variables of each fluid (or phase). This set of equations enables us to have another look at the problem.

The first step consists in building a two-phase flow model in which both phases are compressible. Only a few attempts to do this exist in the literature. They are related to studies on detonation waves in granular materials (Butler *et al*. [7], Powers *et al*. [30], Saurel *et al*. [36]). In these works, the various models were not suitable for solution of interface problems, which is why we have built a new model that allows the treatment of interface problems, as well as homogeneous two-phase flows.

Compressible homogeneous two-phase flows are our second domain of interest. These flows consist in general of a carrier phase (gas or liquid) with suspended or packed particles, droplets, or bubbles. This situation is rather different from that of multifluid flows, where the phases are separated by well-defined interfaces. In multiphase flows, a control volume contains a large number or individual particles (or bubbles, etc.) with many interfaces, while in multifluid flows, nearly all control volumes contain pure phases, except for the
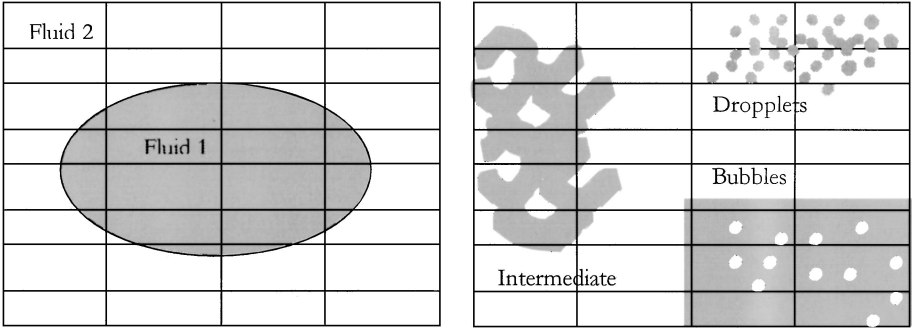
FIG. 1. Schematic representation of a "numerical" multifluid flow (left) and several multiphase flows (right).

computational cells around the interface. The distinction we make between multifluid and multiphase flows can be represented schematically as shown in Fig. 1.

Of course, a multiphase flow can be considered as a multifluid flow with an extremely large number of interfaces. But, for computational purposes, it is better to consider homogenized equations where all physical phenomena occurring in a control volume have been averaged with the help of suitable physical assumptions, and mathematical tools.

The model we develop in this paper follows these principles. It applies both to multifluid flows and to multiphase flows. The model is hyperbolic. It tends to the Euler equations in each pure fluid zone. When summing mass, momentum, and energy equations of the two phases, we get back the Euler equations for the mixture. Our system of partial differential equations cannot be written in conservative form. This drawback usually leads to theoretical and practical difficulties in defining the weak solutions of the problem and in computing them. Here, we develop an original numerical method that relies on knowledge of particular features of some physical solutions. In doing this, we generalize a criterion developed by Abgrall [2] and Saurel and Abgrall [40]. Thanks to this procedure, we are able to adapt methods based on the classical Riemann problem to our problem: the resulting schemes are robust and accurate.

2. WHY MULTISPECIES ALGORITHMS FAIL FOR MULTIFLUID FLOWS

For numerical simulation of multispecies flows, as done, for example, in combustion problems, the model that is used most often is written in terms of mass fraction equations and partial pressures. But the notion of partial pressures is valid only at local thermodynamic equilibrium. When a control volume contains several gases perfectly mixed together, this notion is valid in most cases (in the absence of non-equilibrium effects such as vibration or chemical reactions) because the number of collision between molecules is so large that the temperature is rapidly homogenized. Temperature is homogenized as a result of the occurrence of a large number of collisions between the various molecules. When fluids are not initially well mixed, as when an interface exists, collisions occur only in a tiny part of the control volume: at the interface. So each fluid has its own temperature and the assumption of local thermodynamic equilibrium no longer holds. The numerical errors induced by such an assumption were pointed out by Abgrall [1] on a one-dimensional shock tube test case with two gases of different specific heat ratios. To illustrate what happens with these models, we
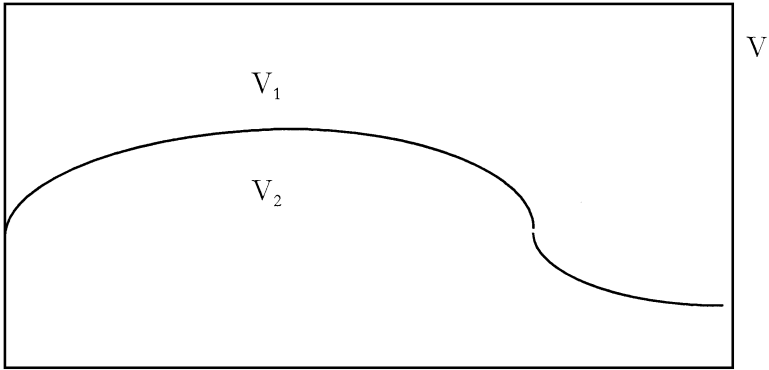
FIG. 2. A two-fluid control volume.

examine a simplified example using the notion of mass fractions and partial pressures. Consider a control volume V filled with a volume V_1 of fluid 1 and a volume V_2 of fluid 2 (Fig. 2).

Volume V_k contains the mass $M_k = n_k \hat{M}_k$, where n_k and $\hat{M}_k$ represent respectively the number of moles and the molar mass of fluid k ($k = 1$ *or* 2). The notion of partial pressures is base d on local thermodynamic equilibrium. In this simplified problem, this yield to consider local thermal equilibrium: $T_k = T$. Partial pressure P_{p1} is the pressure that fluid 1 would have if it occupied all of volume V. Assuming that all fluid is governed by the ideal gas law, and noting that $\hat{R}$ is the molar gas constant (Avogadro constant), we get

$$P_{pk} = n_k \hat{R} T / V. \tag{1}$$

The mixture pressure is defined by $P = \sum P_{pk}$. Equation (1) can be rewritten as

$$P_{pk} = (n_k \hat{M}_k / V)(\hat{R}/\hat{M}_k)T = \rho_{pk} R T, \tag{2}$$

where ρ_{pk} represents the partial density, that is, the density that fluid k would have if it occupied all of volume V. R represents the gas constant per unit mass. The mixture density then reads $\rho = \sum \rho_{pk}$.

It is convenient to introduce mass fractions $Y_k = \rho_{pk}/\rho$. Then the pressure reads

$$P = \rho R T, \tag{3}$$

where the gas constant is $R = \hat{R}/\bar{M}$ with $\bar{M} = 1/\sum(Y_k/\hat{M}_k)$. Imagine now that volume V corresponds to a computational cell in the numerical diffusion zone of a contact discontinuity (or interface). For example, fluid 1 is air and fluid 2 is liquid water. There is no reason why the temperatures of these fluids should be in equilibrium during the numerical diffusion process of the computational method. The same remark holds even if the two fluids are two gases. But the Euler or Navier–Stokes equations provide a single temperature for the mixture, and so force the two fluids to be in thermal equilibrium even if physically it is impossible. This error results in the well-known pressure and velocity oscillations in the shock tube test problem with two gamma (Abgrall [1]).

These indications have caused us to consider another approach, that adopted by scientists working on multiphase flows. This approach is based on the notion of volume fractions, $\alpha_k = V_k/V$. The mixture density is obtained by $\rho = \sum \alpha_k \rho_k$, where the densities of each

phase are defined by $\rho_k = n_k \hat{M}_k / V_k = M_k / V_k$. The pressure of each phase is given by $P_k = \rho_k R_k T_k$ and the mixture pressure is defined by

$$P = \sum \alpha_k P_k. \tag{4}$$

Note that if the temperatures are in equilibrium, $T_k = T$, then the pressure given by (4) is equal to the pressure given by (3). The advantage of the formulation using volume fractions is clear: it is not necessary to have temperature equilibrium to compute the pressure. On the other hand, this formulation necessitates knowledge of the two temperatures or internal energies and also of the two densities. The model that is developed in the following allows determination of these variables.

3. THE TWO-PHASE FLOW MODEL

3.1. Physical Properties

To obtain the two-phase flow model we follow the method and assumptions proposed by Drew [13] for incompressible two-phase flows and apply these principles to compressible flows. For the sake of simplicity we do not detail the various steps before obtaining the following averaged equations. Details may be found in Saurel and Gallouet [42]. We start from the single-phase Navier–Stokes equations in each phase and apply the averaging procedure of Drew. We then neglect all dissipative terms everywhere except at the interfaces.

$$\frac{\partial \alpha_g}{\partial t} + V_i \frac{\partial \alpha_g}{\partial x} = 0 \tag{5a}$$

$$\frac{\partial \alpha_g \rho_g}{\partial t} + \frac{\partial \alpha_g \rho_g u_g}{\partial x} = \dot{m} \tag{5b}$$

$$\frac{\partial \alpha_g \rho_g u_g}{\partial t} + \frac{\partial \left(\alpha_g \rho_g u_g^2 + \alpha_g P_g \right)}{\partial x} = P_i \frac{\partial \alpha_g}{\partial x} + \dot{m} V_i + F_d \tag{5c}$$

$$\frac{\partial \alpha_g \rho_g E_g}{\partial t} + \frac{\partial u_g (\alpha_g \rho_g E_g + \alpha_g P_g)}{\partial x} = P_i V_i \frac{\partial \alpha_g}{\partial x} + \dot{m} E_i + F_d V_i + Q_i \tag{5d}$$

$$\frac{\partial \alpha_l \rho_l}{\partial t} + \frac{\partial \alpha_l \rho_l u_l}{\partial x} = -\dot{m} \tag{5e}$$

$$\frac{\partial \alpha_l \rho_l u_l}{\partial t} + \frac{\partial \left(\alpha_l \rho_l u_l^2 + \alpha_l P_l \right)}{\partial x} = -P_i \frac{\partial \alpha_g}{\partial x} - \dot{m} V_i - F_d \tag{5f}$$

$$\frac{\partial \alpha_l \rho_l E_l}{\partial t} + \frac{\partial u_l (\alpha_l \rho_l E_l + \alpha_l P_l)}{\partial x} = -P_i V_i \frac{\partial \alpha_g}{\partial x} - \dot{m} E_i - F_d V_i - Q_i, \tag{5g}$$

where $\alpha_g + \alpha_l = 1$. The notations are classical. E_k represents the total energy, $E_k = e_k + 1/2u_k^2$.

We have posed that the two-phase flow be composed of gas (subscript g) and liquid (subscript l). The interfacial variables have the subscript i. The left-hand sides of the last six equations are classical. On the right-hand sides of the same equations are terms related to mass transfer $\dot{m}$, drag force F_d, convective heat exchange Q_i, and the non-conservative terms $P_i (\partial \alpha_g / \partial x)$ and $P_i V_i (\partial \alpha_g / \partial x)$. The pressure P_i and the velocity V_i represent averaged

values of the interfacial pressure and velocity over the two-phase control volume. They must be modeled. The gas and liquid pressures are given by appropriate equations of state.

Modeling of the averaged interfacial variables is rather delicate, and we discuss this point in the following sections. Equation (5a) expresses the evolution of the volume fraction and is obtained by the averaging procedure of Drew [13]; see also Saurel and Gallouet [42]. This equation indicates that the volume fraction propagates with the mean interfacial velocity, which is not equal to the local fluid velocity.

The problem now is expressing the various interfacial terms. Mass transfer $\dot{m}$, drag force F_d, and convective heat exchange Q_i are usually given by empirical relations depending on the process under study: evaporation, condensation, combustion, etc. Often, these closure models necessitate determination of characteristic size parameters of individual "particles" constituting the flow: for example, droplet size or bubble size. In this situation, conservation equations for the number density of individual particles may be added (see, for example, Saurel [39]:

$$\frac{\partial N_g}{\partial t} + \frac{\partial N_g u_g}{\partial x} = \dot{N}_g$$
$$\frac{\partial N_l}{\partial t} + \frac{\partial N_l u_l}{\partial x} = \dot{N}_l. \tag{6}$$

The closure laws, $\dot{N}_g$ and $\dot{N}_l$, express fragmentation laws, for example, and are given also by empirical relations. Relations (6) are uncoupled from system (5). So, they do not change its mathematical properties, nor its solution.

The non-conservative terms are always present, whatever the physical processes occurring at the interfaces. Hence their modeling must be independent of the other processes related to mass, momentum, or energy transfers. Their modeling must be achieved carefully in order to obtain a well-posed mathematical model: hyperbolic. Usually, in dealing with two-phase gas–liquid flows, most authors consider the liquid as incompressible. So, they write that the liquid and interfacial pressure equals the gas pressure. This choice yields ill-posed mathematical models. This results in numerical instabilities during numerical solution, or in the necessity of using an extremely large numerical viscosity. Others authors (Toro [46], Sainsaulieu [35]) propose introducing a pressure non-equilibrium effect such as $P_i = P_g + \theta(\alpha_g)$. For Sainsaulieu, $\theta(\alpha_g)$ is a perturbation term that enables the system to be hyperbolic. For Toro, this is a term due to compaction effects in a packed powder bed. Others authors (Powers $et\ al.$ [30]) assume that $P_i = 0$. This non-justifiable choice yields however to a hyperbolic system. In our approach, since we consider each phase as compressible, there is no need to make an artificial choice. A way to estimate the mean interfacial pressure is to consider it equal to the mixture pressure (other estimates are possible),

$$P_i = \sum \alpha_k P_k. \tag{7}$$

The phase pressures P_k are given by appropriate equations of state, $P_k = P_k(e_k, \rho_k)$.

Considering each phase as compressible can be seen as an unrealistic assumption in many two-phase flow problems. However, we are mostly interested in very high pressure flows involving gases, liquids, and solids. Our typical situations are related to detonation problems with high explosives. Under the pressure range in which we are interested, compressibility of each material must be taken into account. However, in the general case, it is always possible

to consider materials, even liquid or solid, as compressible. All materials are compressible, even if in most situations at moderated pressures, compressibility effects of liquids and solids are negligible. Since considering each phase as compressible yields a well-posed model, one can use physically valid equations of state for liquid and solid, or build artificial equations of state for these materials when they behave as incompressible fluids. Of course, this poses new theoretical problems for the building of judicious equations of state, and also numerical difficulties for the solution of the equations. When a liquid or a solid is considered to be compressible and the flow velocity is relatively low, we are facing the difficult problem of low Mach number resolution. We do not enter into these difficulties here. In Section 6, we will show several test problems in which the behavior of incompressible fluids has been reproduced by considering them as compressible. The second difficulty with non-conservative terms and equations lies in the estimate of the averaged interfacial velocity V_i. In most references, V_i is taken equal to the velocity of the incompressible or the less compressible phase (Butler *et al.* [7], Baer and Nunziato [3], Saurel *et al.* [36], Saurel [39], Sainsaulieu [35]). Delhaye and Bouré [12] proposed an estimate for the interface velocity, the velocity of the center volume $V_i = \sum \alpha_k u_k$. We prefer the estimate corresponding to the center of mass velocity. This velocity corresponds to the one where all non-equilibrium systems will relax. In particular, the flow regions where the velocity equilibrium is reached propagate with the center of mass velocity:

$$V_i = \sum \alpha_k \rho_k u_k \Big/ \sum \alpha_k \rho_k. \tag{8}$$

We will come back to the concept of equilibrium state in the following. Keep in mind that our choices for P_i and V_i are only estimates. We will examine the errors induced by such approximations by examining shock solutions in these media. Before doing this, we examine some mathematical properties of the model.

3.2. Mathematical Properties

The following mathematical analysis is done without exchange terms ($\dot{m}$, F_d, Q_i). We consider system (5) written with primitive variables.

$$\frac{\partial W}{\partial t} + A(W)\frac{\partial W}{\partial x} = 0 \tag{9}$$

with $W = (\alpha_g, \rho_g, u_g, P_g, \rho_l, u_l, P_l)^T$ and

$$A(W) = \begin{pmatrix} V_i & 0 & 0 & 0 & 0 & 0 & 0 \\ \frac{\rho_g}{\alpha_g}(V_i - u_g) & u_g & \rho_g & 0 & 0 & 0 & 0 \\ \frac{P_g - P_i}{\alpha_g \rho_g} & 0 & u_g & 1/\rho_g & 0 & 0 & 0 \\ \frac{\rho_g c_{gi}^2}{\alpha_g}(V_i - u_g) & 0 & \rho_g c_g^2 & u_g & 0 & 0 & 0 \\ \frac{\rho_l}{\alpha_i}(V_i - u_l) & 0 & 0 & 0 & u_l & \rho_l & 0 \\ \frac{P_l - P_i}{\alpha_l \rho_l} & 0 & 0 & 0 & 0 & u_l & 1/\rho_l \\ \frac{\rho_l c_{li}^2}{\alpha_l}(V_i - u_l) & 0 & 0 & 0 & 0 & \rho_l c_l^2 & u_l \end{pmatrix},$$

where

$$c_k^2 = \frac{\frac{P_k}{\rho_k^2} - \frac{\partial e_k}{\partial \rho_k}\big|_{P_k}}{\frac{\partial e_k}{\partial P_k}\big|_{\rho_k}} \quad \text{and} \quad c_{ki}^2 = \frac{\frac{P_i}{\rho_k^2} - \frac{\partial e_k}{\partial \rho_k}\big|_{P_k}}{\frac{\partial e_k}{\partial P_k}\big|_{\rho_k}}$$

represent the sound speed of phase k and the sound speed of phase k at the interface, respectively. By comparison with system (5) without the non-conservative terms of Eqs. (5c)–(5f), the only modification lies in the terms multiplied by $\partial \alpha_g / \partial x$ (first column). Thanks to this remark, the matrix A admits real eigenvalues $\lambda_{\text{int}} = V_{\text{int}}$, $\lambda_g^+ = u_g + c_g$, $\lambda_g^- = u_g - c_g$, $\lambda_g^0 = u_g$, $\lambda_l^+ = u_l + c_l$, $\lambda_l^- = u_l - c_l$, $\lambda_l^0 = u_l$. Since they are distinct, A is diagonalizable: the model is strictly hyperbolic (except of course when locally some eigenvalues are degenerate). Moreover, it can be easily shown that our system is frame invariant.

3.3. On the Shock Relations

The analysis of system (5) shows that classical Rankine–Hugoniot relations do not exist for such a system: non-conservative terms are present on the right-hand side of the equations. This is a well-known fact in non-conservative systems of PDE. On the other hand, when the gas volume fraction tends to zero or to unity, we recover the classical Euler equations for each phase for which we have well-known Rankine–Hugoniot relations. Moreover, summation over the two phases of the mass, momentum, and energy equations yields the Euler equations written in mixture variables (mixture density, momentum, and energy). The mixture Euler equations admit well-defined Rankine–Hugoniot relations.

Now, we examine an example that will explain why such a media and equation system does not admit classical Rankine–Hugoniot relations. This example will also show some limitations of the P_i and V_i estimates given by relations (7) and (8). Consider a column filled with liquid containing bubbles. The column is impacted by a high velocity piston on its left side. Since there are no mass, momentum, and energy exchanges between liquid and gas, the exchange surface between phases has no influence. Hence, the liquid column with bubbles can be considered as a separate two-phase flow with an interface, as sketched in Fig. 3b. Since the two fluids are compressible, there are two shock waves that propagate in the liquid and in the gas. Since each fluid has its own physical properties and equations of state, the shock waves have two distinct velocities, and the fluids have two distinct pressures. The two fluids cannot retain this pressure difference for a long period. Transverse waves are propagating in the gas and the liquid in order that pressures may tend toward equilibrium.
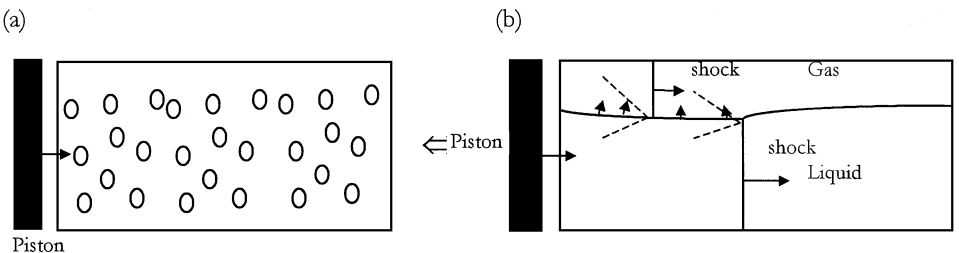

FIG. 3. A liquid column with bubbles impacted by a piston, and its equivalent configuration for the physical model.

During this pressure relaxation process, the interface moves with a two- or three-dimensional motion. After transverse wave propagation, the two shock waves collapse into a single two-dimensional curved wave for the configuration represented in Fig. 3b. In Fig. 3a, the processes detailed previously occur at each bubble interface and the resulting "shock wave" is a very complicated wave affected by the multidimensional microscopic dynamics of bubbles. A one-dimensional average made over these complex waves does not correspond to a classical shock wave.

An experimental study of a situation similar to that represented in Fig. 3a, with gas bubbles in another gas under shock waves, may be found in Haas [21]. Pressure records show clearly a shock wave that does not at all fulfill the Rankine–Hugoniot conditions. A simpler situation with cylindrical or spherical gas bubbles is reported in Haas and Sturtevant [22]. This situation is closer to the one represented in Fig. 3b with refracted shock waves from an interface. Computation of a similar problem with a gas bubble in a liquid may be found in Saurel and Abgrall [40].

Direct simulation of the situation represented in Fig. 3b may be done with the method described in the latter reference. We model exactly the situation represented in this figure with a copper piston impacting the column at 1000 m/s. The computational domain is 1 m long and 0.2 m high. On the first 0.15 m in the y direction we initially set a liquid and on the other 0.05 m we initially set a gas. Liquid (water), gas (air), and copper are modeled by the Stiffened gas equation of state with the parameters given in Saurel and Abgrall [40]. The copper, liquid, and gas densities are initially 8900, 1000, and 100 kg/m^3, respectively. So the initial flow contains densities and material (EOS parameter) discontinuities. For the present computations we use the method described in Saurel and Abgrall [40] with second order variant and exact Riemann solver. The results at time 156 μs are shown Fig. 4. The two distinct shock waves are clearly visible. The liquid shock wave is curved while the gas flow is very difficult to analyze due to the presence of many transverse waves and complex interactions. As predicted, the gas–liquid interface is displaced by a two-dimensional motion in order that the pressure may be uniform.

This multidimensional interface motion has not been taken into account by the definition of mean interface velocity given by (8). Hence corrections terms must be added to system (5) in order to restore the relaxation processes. Before giving details of these relaxation terms, we examine another situation that will point out the need to introduce relaxation terms.

3.4. The Interface Problem

Our goal is to solve homogeneous two-phase flows governed by a set of averaged equations like system (5) as well as an interface problem occurring in multifluid flows. The interfaces we are interested in can separate two pure fluids, or a two-phase mixture and a pure fluid. In one of these applications a fundamental difficulty appears at the interface, during resolution.

Consider, first, an interface separating two pure fluid flows that we want to solve with the two-phase flow equations. In order to use these equations, pure fluids must be modeled as a mixture of the two fluids that contains a negligible amount of one of the fluids. Typically, $\alpha_g = 1 - \varepsilon$ in the gas, and $\alpha_1 = 1 - \varepsilon$ in the liquid with ε of the order of 10^{-6}. The wave configuration at the interface can be sketched as in Fig. 5.

Solid liquid interface   gas   liquid

Copper
piston
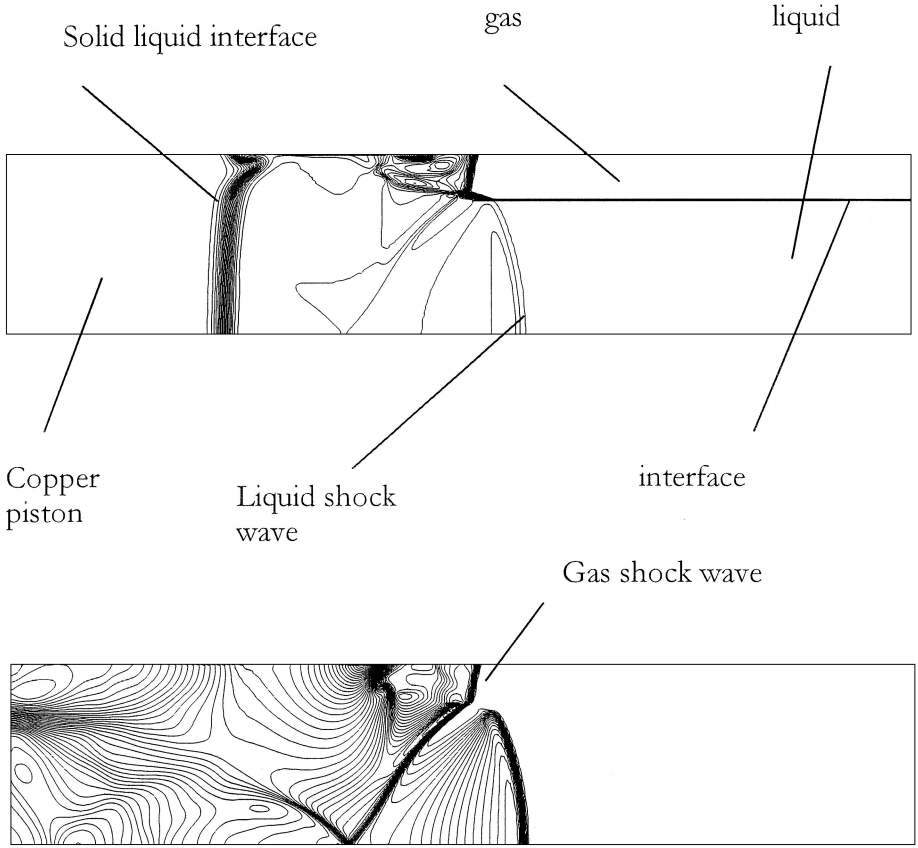
Liquid shock
wave

interface

Gas shock wave

FIG. 4. Numerical simulation of the problem represented in Fig. 3b. *Top*: density contours. *Bottom*: pressure
contours. Time: 156 μs after the impact of the copper plate on the liquid–gas column.

t

λ_g^+ λ_l^+ λ_l^0 λ_{int} λ_g^0 λ_l^- λ_g^-

x

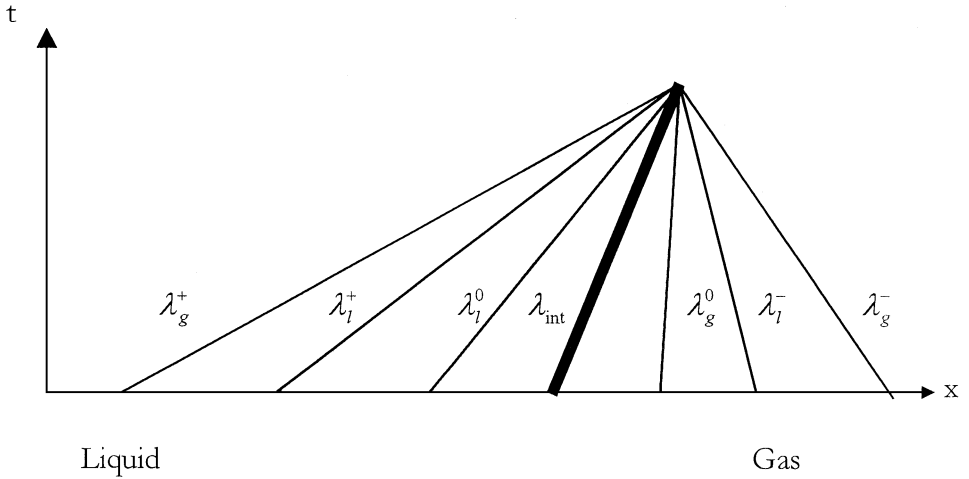Liquid   Gas

FIG. 5. Wave pattern at the interface.

The volume fraction evolves discontinuously across the interface. In particular, as we have mentioned, α_g is close to 1 in the gas, and close to zero in the liquid. Since α_g is close to zero in the liquid, the characteristic direction λ_g^+ propagates a wave with negligible amplitude, which corresponds to a missed wave for the gas system. For the same reason, the characteristic wave λ_l^- is also missing too. Hence, system (5) is not closed at the interface. In the Euler system, this situation is similar to the treatment of a boundary condition where one of the three characteristic directions falls into a vacuum. Here, to close the system two boundary conditions must be supplemented. When the interface separates a two-phase mixture and a pure fluid zone, the problem is similar: one of the two previous characteristic directions is missing.

In the following, we propose closure relations and relaxation terms in order to restore boundary conditions at the interface, and to take into account relaxation pressure process behind shock or pressure waves.

4. CLOSING THE MODEL

We have previously mentioned two particular problems for which the model was ill-adapted:

—relaxation phenomena behind shock and pressure waves in two-phase mixtures,
—interface conditions between pure fluids or mixtures.

We now examine separate ways to solve these problems, and we will show that it is possible to derive a general formulation.

4.1. Pressure Relaxation and Interface Pressure Condition

Pressure relaxation.   We first reexamine the problem schematized in Fig. 3. After propagation of the shock waves, the system will evolve after a more or less lengthy time period to an equilibrium state where

$$
\begin{aligned}
&P_g - P_l = 0 && \text{if the two fluids are perfect,} \\
&P_g + \frac{2\sigma}{R} - P_l = 0 && \text{if the surface tension effects are considered (σ represents} \\
&&& \quad \text{the surface tension and R the bubble radius),} \\
&P_g + \tilde{T}(\alpha_g) - P_l = 0 && \text{if the two-phase mixture is composed of solid packed} \\
&&& \quad \text{powder grains and gas.}
\end{aligned}
\tag{10}
$$

$\tilde{T}(\alpha_g)$ represents the intergranular stress tensor. It is due to contact stresses between particles under packing (Toro [46], Saurel *et al.* [36]).

In the following, for the sake of clarity, we no longer consider the effects due to surface tension or to the intergranular stress tensor.

After wave propagation, the fluids are in a non-equilibrium pressure state ($P_g \neq P_l$) and a pressure relaxation process will develop so that pressure will tend to equilibrium, $P_g = P_l$. Locally, after the wave propagation, the fluids undergo a two- or three-dimensional motion as represented in Fig. 3. This 2D or 3D motion, at microscopic scale (bubble scale, for example) creates a volume variation of each fluid, accompanied by an internal energy variation, so that pressures tends to equilibrium. This motion is due to the 3D propagation of the various waves. As indicated by Baer and Nunziato [3], this complex motion

can be summarized by a homogenization variable that expresses the velocity at which pressure equilibrium is reached. This homogenization variable μ (dynamic compaction viscosity) depends on the compressibility of each fluid (and so of their equations of state), on the nature of each fluid, and on the two-phase mixture topology. Existence of this variable has been shown theoretically, following the second law of thermodynamics and mechanics of irreversible processes, by Baer and Nunziato [3]. Experimental measurement of this variable has been done by Baer [4] for a medium composed of polyurethane foam.

Locally, after wave propagation, the pressure relaxation process undergoes a volume variation given by the equation

$$\frac{\partial \alpha_g}{\partial t} = \mu (P_g - P_i). \tag{11}$$

This volume variation induces energy variations due to the interfacial pressure work:

$$\frac{\partial \alpha_g \rho_g E_g}{\partial t} = -\mu P_i (P_g - P_l)$$

$$\frac{\partial \alpha_l \rho_l E_l}{\partial t} = -\mu P_i (P_g - P_l). \tag{12}$$

The dynamic compaction viscosity μ is a positive coefficient or a more complicated positive function $(\mathrm{Pa}^{-1}\,\mathrm{s}^{-1})$. The right-hand side of Eq. (12) represents the pressure work during the pressure relaxation process.

Pressure interface condition.   We now reexamine the wave pattern occurring at the interface when two-phase flow equations are solved (Fig. 5). We have seen that two characteristic directions were missed, corresponding to an ill-posed moving boundary problem. It is well known that the interface pressure condition under two pure fluids consists in equality of pressure across the interface. When two-phase flow equations are solved, the two fluids are mixed initially and mixed again by the numerical diffusion at the interface. Hence, to restore the pressure interface condition, it is necessary to impose pressure equality between phases: $P_g = P_l$. It is important to note that this condition corresponds to the equilibrium condition (10) after pressure relaxation in the two-phase mixture. Thus, it is possible to force pressure equality at the interface, after wave propagation, by solving the same system as that proposed previously, (11)–(12). However, since pressure equality must be satisfied at each time, it is necessary that the pressure relaxation be instantaneous, so that the dynamic compaction viscosity tends to infinity. When the interface separates a two-phase mixture and a single-phase fluid, the pressure equality condition is still valid. The previous procedure is unchanged.

To summarize, the wave dynamics in the two-phase mixture or at the interface is given by system (5). The relaxation pressure process in the two-phase mixture and the interface conditions are given by system (11)–(12) . The terms appearing in system (11)–(12) must be added to system (5). The dynamic compaction viscosity has a finite value in the two-phase zones, while it becomes infinite at the interface. When the right-hand side of Eq. (11) is added to the first equation of system (5), the term $\mu (P_g - P_l)$ can be also considered as a correction for the 1D estimate of the interfacial velocity given by (8), accounting for the 2D or 3D interfacial or microscopic motion.

4.2. Velocity Relaxation and Interface Velocity Condition

The velocity relaxation process in the two-phase mixture may have a long characteristic time compared to that of the pressure relaxation. On one hand it depends on the pressure relaxation process, which in general is fast compared to the longitudinal wave propagation dynamics; on the other hand it depends on effects related to fluid viscosity. These last effects may be very slow compared to the others. The velocity relaxation process has already been expressed in Eqs. (5). Terms related to the drag force F_d are responsible for it. The drag force may be written in the same form as the pressure relaxation term: a relaxation coefficient multiplied by the velocity difference

$$F_d = \lambda(u_l - u_g), \tag{13}$$

where λ is a positive parameter or function. In two-phase flow zones, λ has a finite value.

We now consider the interface problem. When the interface separates two pure fluids, the second interface condition imposes velocity equality at the interface. By the same reasoning as that for pressures, it implies that fluid velocities are in equilibrium: $u_g = u_l$. A way to impose this condition, and consequently to restore the missed characteristic direction, is to solve system (5) with the drag force and an infinite velocity relaxation coefficient λ. When the interface separates a two-phase medium and a pure fluid, this condition no longer applies. The drag force then furnishes information on the velocity difference between phases. This can be considered as a closure relation at the interface.

Summary

To summarize, the overall system that must be solved can be written as

$$\frac{\partial \alpha_g}{\partial t} + V_i \frac{\partial \alpha_g}{\partial x} = \qquad\qquad \mu(P_g - P_l)$$

$$\frac{\partial \alpha_g \rho_g}{\partial t} + \frac{\partial \alpha_g \rho_g u_g}{\partial x} = 0$$

$$\frac{\partial \alpha_g \rho_g u_g}{\partial t} + \frac{\partial \left(\alpha_g \rho_g u_g^2 + \alpha_g P_g\right)}{\partial x} = P_i \frac{\partial \alpha_g}{\partial x} \qquad\qquad + \lambda(u_l - u_g)$$

$$\frac{\partial \alpha_g \rho_g E_g}{\partial t} + \frac{\partial u_g(\alpha_g \rho_g E_g + \alpha_g P_g)}{\partial x} = P_i V_i \frac{\partial \alpha_g}{\partial x} \quad + \mu P_i(P_g - P_l) \;\; + \lambda V_i(u_l - u_g)$$

$$\frac{\partial \alpha_l \rho_l}{\partial t} + \frac{\partial \alpha_l \rho_l u_l}{\partial x} = 0 \tag{14}$$

$$\frac{\partial \alpha_l \rho_l u_l}{\partial t} + \frac{\partial \left(\alpha_l \rho_l u_l^2 + \alpha_l P_l\right)}{\partial x} = -P_i \frac{\partial \alpha_g}{\partial x} \qquad\qquad - \lambda(u_l - u_g)$$

$$\frac{\partial \alpha_l \rho_l E_l}{\partial t} + \frac{\partial u_l(\alpha_l \rho_l E_l + \alpha_l P_l)}{\partial x} = -P_i V_i \frac{\partial \alpha_g}{\partial x} \quad - \mu P_i(P_g - P_l) \;\; - \lambda V_i(u_l - u_g)$$

| Hyperbolic system | Pressure relaxation | Velocity relaxation |

Interface conditions

Mass and energy transfer terms have been omitted. They are not essential and are mentioned in system (5). The system is thus composed of a hyperbolic part, supplemented by pressure

relaxation terms to account for the microscopic motion behind the pressure waves and the pressure interface condition, and velocity relaxation terms, to account for drag forces in the two-phase mixture, and the velocity interface condition. The relaxation parameters are positive. The dynamic compaction viscosity μ is finite within two-phase flow regions, and infinite at the interface. If pressure non-equilibrium effects are not interesting from a physical point of view, the parameter μ can be assumed to be infinite in the two-phases mixture too. The same remark stands for the relaxation velocity coefficient λ.

We will see in the following how to solve the equations when the relaxation parameters λ and μ tend to infinity.

In many physical situations, it is reasonable to assume that pressure tends to equilibrium instantaneously. This corresponds to an infinite value of the μ parameter. In this context, the solution is evolved over time by solution of a strictly hyperbolic system, followed by a pressure relaxation step. This is completely different from assuming pressure equilibrium in the original equations and trying to solve such equations. When such an assumption is made, the corresponding system is not hyperbolic, and the solution is not accurate. In particular, with interface problems in which the volume fraction varies discontinuously, such a model with a single pressure would fail at the second time step.

So, our approach is close to that followed in gaseous reacting flows:

—solution of the gas dynamic equations with a hyperbolic solver;
—integration of the chemical kinetics effects, or calculation of local thermodynamic equilibrium to find thermodynamic properties and composition of the gas mixture.

Here, we solve:

—the two-phase flow equations with a hyperbolic solver;
—pressure and velocity relaxation effects, or assume instantaneous pressure equilibrium.

We begin in the next section by first detailing the hyperbolic solver.

5. THE NUMERICAL METHOD

The numerical method we develop here applies at mesh point: single-phase, two-phase, and at the interfaces. For the sake of simplicity and generality regarding complex equations of state for the various fluids, we have retained the simplest ingredients for the construction of a high-resolution scheme for two-phase flows with arbitrary equations of state. Riemann solvers are chosen for easy implementation with various models and equations of state, even though their accuracy is imperfect. We have excluded accurate but overcomplex Riemann solvers as presented in Saurel *et al.* [37]. More accurate handling of the mathematical properties of our two-phase flow models could probably be done with the approximate Roe solver following Sainsaulieu [35]. Another method, both simple and accurate, could be examined and extended for the seven-equation model: the Gallouet and Masella method [17]. Here, classical ingredients are retained.

The model we propose is hyperbolic. In particular, the same techniques as those for single-phase gas dynamics equations can be used. However, the hyperbolic systems involve non-conservative terms and a non-conservative equation (the volume fraction evolution equation). Their solution poses particular problems. Here, we reuse the basic idea of Abgrall [2] and apply it to non-conservative systems. We showed previously that numerical

schemes that fulfill the basic criterion of Abgrall [2] were able to solve simplified multifluid problems (Saurel and Abgrall [40]). Here, this criterion provides an accurate and robust discretisation scheme for non-conservative terms and volume fraction evolution equation. We examine the method in 1D, with a first order numerical scheme. The solution is obtained by a succession of operators (Strang [45]),

$$U_i^{n+1} = L_s^{\Delta t} L_h^{\Delta t} U_i^n,$$

where $L_h^{\Delta t}$ denotes the hyperbolic operator, containing non-conservative terms, and $L_s^{\Delta t}$ denotes the integration operator for source and relaxation terms.

First, we examine the hyperbolic operator, which poses the main difficulties.

5.1. Hyperbolic Operator

The major idea that serves as a guide for the building of the numerical scheme is a generalization of the Abgrall [2] criterion. It is stated as follows: "A two phase flow, uniform in pressure and velocity must remain uniform on the same variables during its temporal evolution." It can be shown in system (14) that if $u = u_g = u_l = V_i$ as well as $P = P_g = P_l = P_i$ is uniform at time $t = 0$, then the velocities and the pressure will keep the same values. Consider, for example, system (14), under the primitive variable formulation (9). Since $u = u_g = u_l = V_i$ and $P = P_g = P_l = P_i$ most spatial derivative terms cancel and we get

$$\frac{\partial \alpha_g}{\partial t} + u \frac{\partial \alpha_g}{\partial x} = 0; \qquad \frac{\partial \rho_g}{\partial t} + u \frac{\partial \rho_g}{\partial x} = 0; \qquad \frac{\partial u_g}{\partial t} = 0; \qquad \frac{\partial P_g}{\partial t} = 0;$$

$$\frac{\partial \rho_l}{\partial t} + u \frac{\partial \rho_l}{\partial x} = 0; \qquad \frac{\partial u_l}{\partial t} = 0; \qquad \frac{\partial P_l}{\partial t} = 0.$$

It is clear that no pressure or velocity variations appear.

This guide has been systematically exploited in the context of the Euler equation and has shown that it provides an efficient discretisation scheme for non-conservative equations even when velocity and pressure are not initially uniform (Saurel and Abgrall [40]). Indeed, all non-equilibrium system will relax to an equilibrium state where velocities and pressures are locally uniform.

Modification of the Godunov–Rusanov Scheme

As in Saurel and Abgrall [40], we reuse the essential elements for the building of a Godunov-type scheme with a flux function that we want to be simple as possible. This is necessary for a better understanding of the basic ideas. So the numerical flux we have retained is that of Rusanov [34]. In a later section, we will develop another method with a more accurate flux function.

We consider only the first four equations of system (14). The last three equations of the seven-equation model represent a subsystem identical to the last three equations of the submodel with four equations. The system under consideration reads (we suppress the indexes g and l)

$$\frac{\partial \alpha}{\partial t} + V_i \frac{\partial \alpha}{\partial x} = 0$$

$$\frac{\partial U}{\partial t} + \frac{\partial F(U)}{\partial x} = H(U) \frac{\partial \alpha}{\partial x} \tag{15}$$

with $U = (\alpha\rho, \alpha\rho u, \alpha\rho E)^T$, $F = (\alpha\rho u, \alpha\rho u^2 + \alpha P, u(\alpha\rho E + \alpha P))^T$, and $H = (0, P_i,$ $P_i V_i)^T$. We consider a constant mesh spacing Δx. The solution is evolved with a constant time step Δt. The Godunov scheme reads

$$U_i^{n+1} = U_i^n - \frac{\Delta t}{\Delta x}\left(F_{i+1/2}^n - F_{i-1/2}^n\right) + \Delta t H(U_i^n)\Delta, \tag{16}$$

where Δ represents the discrete form of the term $\partial\alpha_g/\partial x$. The numerical flux for the conservative fluxes is given by the Rusanov [34] formula

$$F_{i+1/2}^n = F(U_i, U_{i+1}) = \tfrac{1}{2}\left(F_i + F_{i+1} - S(U_{i+1} - U_i)\right), \tag{17}$$

where $S = \max\{|\lambda_i^+|, |\lambda_i^-|, |\lambda_{i+1}^+|, |\lambda_{i+1}^-|\}$. We now assume that the velocity and pressure are uniform. We note that $\lambda = \Delta t/\Delta x$ and we decompose the various operations made by the numerical scheme over a time step. For the mass conservation equation, after noting that the velocity is uniform, we get

$$\alpha\rho_i^{n+1} = \alpha\rho_i^n - \lambda/2\left[u\left(\alpha\rho_{i+1}^n - \alpha\rho_{i-1}^n\right) - S_{i+1/2}\left(\alpha\rho_{i+1}^n - \alpha\rho_i^n\right) + S_{i-1/2}\left(\alpha\rho_i^n - \alpha\rho_{i-1}^n\right)\right]. \tag{18}$$

With the same development for the momentum equation, we obtain

$$\begin{aligned}\alpha\rho u_i^{n+1} = \alpha\rho u_i^n - \lambda/2\big[&\left((\alpha\rho u^2 + \alpha P)_{i+1}^n - (\alpha\rho u^2 + \alpha P)_{i-1}^n\right) \\ &- S_{i+1/2}\left(\alpha\rho u_{i+1}^n - \alpha\rho u_i^n\right) + S_{i-1/2}\left(\alpha\rho u_i^n - \alpha\rho u_{i-1}^n\right)\big] + \Delta t P\Delta. \end{aligned} \tag{19}$$

If (18) and (19) are combined and the uniformity of pressure and velocity is used, it appears that

$$u_i^{n+1} = u \tag{20}$$

if

$$\Delta = \left(\alpha_{i+1}^n - \alpha_{i-1}^n\right)/(2 \cdot \Delta x). \tag{21}$$

The simple central difference formula (21) provides the numerical scheme for the discretisation of the non-conservative term, when the conservative fluxes are given by the Rusanov flux function. We will see, henceforth, that for another flux function, the discretisation of the non-conservative term is not so simple, and depends on the choice of the flux function for the conservative fluxes.

We now consider the energy equation

$$\begin{aligned}\alpha\rho E_i^{n+1} = \alpha\rho E_i^n - \lambda/2\big[&\left((\alpha\rho Eu + \alpha Pu)_{i+1}^n - (\alpha\rho Eu + \alpha Pu)_{i-1}^n\right) \\ &- S_{i+1/2}\left(\alpha\rho E_{i+1}^n - \alpha\rho E_i^n\right) + S_{i-1/2}\left(\alpha\rho E_i^n - \alpha\rho E_{i-1}^n\right)\big] \\ &+ \lambda/2 Pu\left(\alpha_{i+1}^n - \alpha_{i-1}^n\right). \end{aligned} \tag{22}$$

Using (18), (20), and pressure uniformity we get for the internal energy

$$\begin{aligned}\alpha\rho e_i^{n+1} = \alpha\rho e_i^n - \lambda/2\big[&u_i^n\left(\alpha\rho e_{i+1}^n - \alpha\rho e_{i-1}^n\right) - S_{i+1/2}\left(\alpha\rho e_{i+1}^n - \alpha\rho e_i^n\right) \\ &+ S_{i-1/2}\left(\alpha\rho e_i^n - \alpha\rho e_{i-1}^n\right)\big]. \end{aligned} \tag{23}$$

We now use the equation of state. The pressure of each fluid is given by an equation of state $P_k = P_k(e_k, \rho_k)$. Heuzé [25] showed that nearly all equations of state can be written under the Mie–Gruneisen form

$$P = (\gamma(\rho) - 1)\rho e - \gamma(\rho)\pi(\rho). \tag{24}$$

The Mie–Gruneisen EOS can be written as

$$\rho e = \beta(\rho)P + \eta(\rho) \tag{25}$$

with $\beta = 1/(\gamma - 1)$ and $\eta = \gamma\pi/(\gamma - 1)$. We now replace the product of density and internal energy in Eq. (23) by expression (25):

$$
\begin{aligned}
\alpha(\beta P + \eta)_i^{n+1} &= \alpha(\beta P + \eta)_i^n - \lambda/2\big[u_i^n\big(\alpha(\beta P + \eta)_{i+1}^n - \alpha(\beta P + \eta)_{i-1}^n\big) - S_{i+1/2}\big(\alpha(\beta P + \eta)_{i+1}^n \\
&\quad - \alpha(\beta P + \eta)_i^n\big) + S_{i-1/2}\big(\alpha(\beta P + \eta)_i^n - \alpha(\beta P + \eta)_{i-1}^n\big)\big].
\end{aligned}
$$

In the particular case of the ideal gas EOS or the Stiffened gas EOS, the parameters β and η are constants in each fluid. We then get $P_i^{n+1} = P$, under the condition

$$\alpha_i^{n+1} = \alpha_i^n - \lambda/2\big[u_i^n\big(\alpha_{i+1}^n - \alpha_{i-1}^n\big) - S_{i+1/2}\big(\alpha_{i+1}^n - \alpha_i^n\big) + S_{i-1/2}\big(\alpha_i^n - \alpha_{i-1}^n\big)\big]. \tag{26}$$

Equation (26) gives the numerical scheme that must be used to solve the first equation of system (14), the non-conservative equation. It is easy to note, in scheme (26), the classical dicretised form of the convective term $u_i^n(\alpha_{i+1}^n - \alpha_{i-1}^n)$. The others terms, $-S_{i+1/2}(\alpha_{i+1}^n - \alpha_i^n) + S_{i-1/2}(\alpha_i^n - \alpha_{i-1}^n)$, represent a viscosity term, which is a direct function of the viscosity of the flux function used for the conservative terms. It can also be noticed that this scheme is identical to the one obtained by Saurel and Abgrall [40] for determining the equation of state parameters inside the numerical diffusion zone of an interface separating two materials and a model based on the Euler equations. So, by a very different approach we recover the same scheme, used here for the computation of the volume fraction. It can be shown, but it is not the purpose of the present paper, that the method first proposed in Abgrall [2] and Saurel and Abgrall [40] is included in the present approach, in a more general context.

In the general case of the Mie–Gruneisen EOS, the coefficients β and η are functions of density. To derive a numerical scheme, we assume that these coefficients are local constants. Indeed, density spatial variations in the multiphase formulation are in general relatively weak. It is common for conservative variables such as $(\alpha\rho)$ to have large variations (in particular at an interface), but these variations are due essentially to large variations in α but not in ρ. This is even more true when the flow is uniform in velocity and pressure. For example, when an interface separates two single-phase media, α varies from 0 to 1 in the numerical diffusion zone. In fact, as previously mentioned, our model is valid only when α varies from ε to $1-\varepsilon$ (ε being of the order of 10^{-6}). Inside the numerical diffusion zone, the density of the fluid under consideration will be between the densities of the same fluid on the

right and left sides of the interface. These densities are in general relatively close, because we stay in the same fluid. For example, if the zone where $\alpha = 1 - \varepsilon$ contains essentially a high density liquid, the opposite zone, where $\alpha = \varepsilon$, contains a volume faction ε of the same fluid at the same density (or relatively close). Under these assumptions, Eq. (26) is an accurate approximation of the first equation of system (14). We will see, in several test problems where coefficients β and η are functions of density, that accuracy is sufficient to obtain reliable results.

To summarize, when the Rusanov numerical flux replaces the conservative flux, the resulting scheme reads

$$U_i^{n+1} = U_i^n - \frac{\Delta t}{\Delta x}\left(F_{i+1/2}^n - F_{i-1/2}^n\right) + \Delta t H\left(U_i^n\right)\Delta$$

with

$$F_{i+1/2}^n = F(U_i, U_{i+1}) = \frac{1}{2}(F_i + F_{i+1} - S(U_{i+1} - U_i)),$$

$$\Delta = \left(\alpha_{i+1}^n - \alpha_{i-1}^n\right)/(2 \cdot \Delta x),$$

(27)

and

$$\alpha_i^{n+1} = \alpha_i^n - \lambda/2\left[u_i^n\left(\alpha_{i+1}^n - \alpha_{i-1}^n\right) - S_{i+1/2}\left(\alpha_{i+1}^n - \chi_i^n\right) + S_{i-1/2}\left(\alpha_i^n - \alpha_{i-1}^n\right)\right].$$

Modification of the Godunov–HLL Scheme

In this section, we show how to modify the Godunov scheme when the HLL approximate Riemann solver is used (Harten *et al.* [23]). The numerical flux in the HLL approximation reads

$$F_{\text{HLL}} = \frac{S^+ F_{\text{L}} - S^- F_{\text{R}} + S^+ S^-(U_{\text{R}} - U_{\text{L}})}{S^+ - S^-}.$$

(28)

The indexes R and L are related to the right and left sides of a cell boundary ($i \pm 1/2$). Various choices are possible for the wave speed estimates; see Toro [48], for example. Here we use the Davis [11] estimates

$$S^+ = \max\{0, \lambda_l^+, \lambda_r^+\}; \qquad S^- = \max\{0, \lambda_l^-, \lambda_r^-\}.$$

Following exactly the same developments that we followed with the Rusanov flux function, we get

$$U_i^{n+1} = U_i^n - \frac{\Delta t}{\Delta x}\left(F_{i+1/2}^n - F_{i-1/2}^n\right) + \Delta t H\left(U_i^n\right)\Delta$$

with

$$F_{i+1/2} = \frac{S_{i+1/2}^+ F_i - S_{i+1/2}^- F_{i+1} + S_{i+1/2}^+ S_{i+1/2}^-(U_{i+1} - U_i)}{S_{i+1/2}^+ - S_{i+1/2}^-},$$

$$\Delta = \frac{1}{\Delta x}\left[\frac{S_{i+1/2}^+ \alpha_i^n - S_{i+1/2}^- \alpha_{i+1}^n}{S_{i+1/2}^+ - S_{i+1/2}^-} - \frac{S_{i-1/2}^+ \alpha_{i-1}^n - S_{i-1/2}^- \alpha_i^n}{S_{i-1/2}^+ - S_{i-1/2}^-}\right],$$

(29)

and

$$\alpha_i^{n+1} = \alpha_i^n - \lambda \left[\left\{ u_i^n \left(S_{i+1/2}^+ \alpha_i^n - S_{i+1/2}^- \alpha_{i+1}^n \right) + S_{i+1/2}^+ S_{i+1/2}^- \left(\alpha_{i+1}^n - \alpha_i^n \right) \right\} \right/$$
$$(S_{i+1/2}^+ - S_{i+1/2}^-) - \left\{ u_i^n \left(S_{i-1/2}^+ \alpha_{i-1}^n - S_{i-1/2}^- \alpha_i^n \right) \right.$$
$$\left. + S_{i-1/2}^+ S_{i-1/2}^- \left(\alpha_i^n - \alpha_{i-1}^n \right) \right\} / (S_{i-1/2}^+ - S_{i-1/2}^-) \right].$$

It appears clear that the discretisation of the non-conservative terms and equation strongly depends on the flux function used for the computation of the conservative fluxes.

Extension to Second Order

Extension to second order is done following the basic ideas of Van Leer [50]. The flow variables are characterized by a mean value U_i^n and a slope δU_i^n. In order to preserve a uniform solution regarding pressure and velocity at the end of the predictor step of the van Leer scheme, it is necessary to perform this step with the primitive variable formulation. So, we consider primitive variable vector W_i^n and associated slopes δW_i^n.

When the flow is uniform in velocity and pressure, the u and P slopes are zero. The primitive variables on a cell boundary are computed by

$$W_{i\pm 1/2, \mp}^{n+1/2} = W_i^n \pm 1/2 \, \delta W_i^n - \Delta t / 2 A \left(W_i^n \right) \delta W_i^n. \tag{30}$$

This automatically satisfies the conditions of pressure and velocity uniformity at time $t^{n+1/2}$. The conservative variable vector is then deduced from the primitive one. The corrector step, when the HLL Riemann solver is used, then reads

$$U_i^{n+1} = U_i^n - \lambda \left(F \left(U_{i+1/2,-}^{n+1/2}, U_{i+1/2,+}^{n+1/2} \right) - F \left(U_{i-1/2,-}^n, U_{i-1/2,+}^n \right) \right) + \Delta t H \left(U_i^{n+1/2} \right) \Delta$$

with

$$\Delta = \frac{1}{\Delta x} \left[\frac{S_{i+1/2}^+ \alpha_{i+1/2,-}^{n+1/2} - S_{i+1/2}^- \alpha_{i+1/2,+}^{n+1/2}}{S_{i+1/2}^+ - S_{i+1/2}^-} - \frac{S_{i-1/2}^+ \alpha_{i-1/2,-}^{n+1/2} - S_{i-1/2}^- \alpha_{i-1/2,+}^{n+1/2}}{S_{i-1/2}^+ - S_{i-1/2}^-} \right] \tag{31}$$

and

$$\alpha_i^{n+1} = \alpha_i^n - \lambda \left[\left\{ u_i^{n+1/2} \left(S_{i+1/2}^+ \alpha_{i+1/2,-}^{n+1/2} - S_{i+1/2}^- \alpha_{i+1/2,+}^{n+1/2} \right) + S_{i+1/2}^+ S_{i+1/2}^- \left(\alpha_{i+1/2,+}^{n+1/2} \right. \right. \right.$$
$$\left. - \alpha_{i+1/2,-}^{n+1/2} \right) \right\} / (S_{i+1/2}^+ - S_{i+1/2}^-) - \left\{ u_i^{n+1/2} \left(S_{i-1/2}^+ \alpha_{i-1/2,-}^{n+1/2} - S_{i-1/2}^- \alpha_{i-1/2,+}^{n+1/2} \right) \right.$$
$$\left. \left. + S_{i-1/2}^+ S_{i-1/2}^- \left(\alpha_{i-1/2,+}^{n+1/2} - \alpha_{i-1/2,-}^{n+1/2} \right) \right\} / (S_{i-1/2}^+ - S_{i-1/2}^-) \right].$$

This scheme is stable under the standard CFL condition, based on the largest absolute wave speed.

5.2. Source and Relaxation Operators

In the previous sections, we developed the resolution procedure for the hyperbolic systems, without accounting for source and relaxation terms. The relaxation terms are particularly important since they allow solution of the boundary conditions, at the interface. This step is of paramount importance.

First, recall that the complete solution is obtained by the succession of operators

$$U_i^{n+1} = L_s^{\Delta t} L_h^{\Delta t} U_i^n,$$

when the hyperbolic solver is first order, and

$$U_i^{n+1} = L_s^{\Delta t/2} L_h^{\Delta t} L_s^{\Delta t/2} U_i^n,$$

when the hyperbolic solver is second order (Strang [45]). We now give details of the operator L_s. It approximates the solution of an ordinary differential system. For system (14), when mass and energy transfer terms are considered, it reads

$$\frac{\partial U}{\partial t} = S(U)$$

$$U = (\alpha_g, \alpha_g \rho_g, \alpha_g \rho_g u_g, \alpha_g \rho_g E_g, \alpha_l \rho_l, \alpha_l \rho_l u_l, \alpha_l \rho_l E_l)^T \qquad (32)$$

$$S(U) = (\mu(P_g - P_l), \dot{m}, \lambda(u_l - u_g) + \dot{m} V_i, V_i \lambda(u_l - u_g) - P_i \mu(P_g - P_l) + \dot{m} E_i,$$
$$-\dot{m}, -\lambda(u_l - u_g) - \dot{m} V_i, -V_i \lambda(u_l - u_g) + P_i \mu(P_g - P_l) - \dot{m} E_i)^T.$$

For the sake of clarity, we decompose $S(U)$ into three vectors containing the various source terms,

$$S(U) = MH(U) + V(U) + PR(U), \qquad (33)$$

where $MH(U) = (0, \dot{m}, \dot{m} V_i, \dot{m} E_i + Q_i, -\dot{m}, -\dot{m} V_i, -\dot{m} E_i - Q_i)^T$ is associated with mass and heat transfer, while $V(U) = (0, 0, \lambda(u_l - u_g), V_i \lambda(u_l - u_g), 0, -\lambda(u_l - u_g), -V_i \lambda(u_l - u_g))^T$ is associated with the velocity non-equilibrium terms and the pressure non-equilibrium terms are grouped in

$$PR(U) = (\mu(P_g - P_l), 0, 0, -P_i \mu(P_g - P_l), 0, 0, P_i \mu(P_g - P_l))^T.$$

Solution of the differential problem (32) can be considered to be succession of three integration operators $L_{MH}^{\Delta t}$, $L_V^{\Delta t}$, and $L_{PR}^{\Delta t}$, associated with the corresponding source vectors. The solution of problem (32) is then given by

$$U_i^{n+1} = L_{MH}^{\Delta t} L_V^{\Delta t} L_{PR}^{\Delta t} U_i^n. \qquad (34)$$

In general, mass transfer and heat exchange terms are given by finite rate physical laws. So, the operator L_{MH} consists in an appropriate differential integrator for solving the ODE system involving mass and heat exchanges terms.

When the velocity and pressure related source terms involve finite rate law, finite λ and μ, integration can be performed with the same kind of ODE solver. The distinction appears when λ or μ is infinite. The source terms are now relaxation terms. These coefficients are infinite when we are dealing, for example, with an interface, as previously mentioned. We now describe the method for solving these ODE problems with infinite relaxation coefficients.

Instantaneous Velocity Relaxation

When λ is infinite (instantaneous velocity relaxation), solution of the integration problem $U_i^{n+1} = L_V^{\Delta t} U_i^n$ possesses the following analytic solution. The ODE system to consider can be written in full as

$$\frac{\partial \alpha_g}{\partial t} = 0$$

$$\frac{\partial \alpha_g \rho_g}{\partial t} = 0$$

$$\frac{\partial \alpha_g \rho_g u_g}{\partial t} = \lambda(u_l - u_g)$$

$$\frac{\partial \alpha_g \rho_g E_g}{\partial t} = \lambda V_i(u_l - u_g) \qquad (35)$$

$$\frac{\partial \alpha_l \rho_l}{\partial t} = 0$$

$$\frac{\partial \alpha_l \rho_l u_l}{\partial t} = -\lambda(u_l - u_g)$$

$$\frac{\partial \alpha_l \rho_l E_l}{\partial t} = -\lambda V_i(u_l - u_g).$$

Combination of the mass and momentum equations for each phase yields the differential system

$$\frac{\partial u_g}{\partial t} = \lambda(u_l - u_g)/\alpha_g \rho_g \qquad (36)$$

$$\frac{\partial u_l}{\partial t} = -\lambda(u_l - u_g)/\alpha_l \rho_l. \qquad (37)$$

Subtracting Eq. (36) from Eq. (37) and integrating yield the result

$$u_i - u_g = (u_{l0} - u_{g0}) \exp\left(-\lambda \left[\frac{1}{\alpha_g \rho_g} + \frac{1}{\alpha_l \rho_l}\right] t\right),$$

where variables with the subscript 0 represent the solution obtained after the hyperbolic step (or previous source steps). The solution of this equation when λ tends to infinity for a finite time incremental t is the same as considering a finite value for λ and looking at the steady state solution. Since λ is a positive parameter, the solution is obvious:

$$u_l - u_g = 0. \qquad (38)$$

Now, summing Eqs. (36) and (37) gives

$$\alpha_g \rho_g \frac{\partial u_g}{\partial t} + \alpha_l \rho_l \frac{\partial u_l}{\partial t} = 0.$$

Integration of this equation yields the result

$$\alpha_g \rho_g (u_g - u_{g0}) + \alpha_l \rho_l (u_l - u_{l0}) = 0. \qquad (39)$$

The variables with index 0 represent the solution obtained after solution of the hyperbolic system. Now, using (38) in (39) gives the relaxed solution for the velocities:

$$u = u_g = u_l = \frac{\alpha_g \rho_g u_{g0} + \alpha_l \rho_l u_{l0}}{\alpha_g \rho_g + \alpha_l \rho_l}. \tag{40}$$

This result justifies the choice made for the mean interface velocity V_i (Eq. (8)) since it corresponds to the equilibrium velocity of the two-phase system.

It now remains to account for velocity changes of the total and internal energies of each phase. Indeed, the energy equations contain velocity relaxation terms

$$\frac{\partial \alpha_k \rho_k E_k}{\partial t} = \pm \lambda V_i (u_l - u_g).$$

By combining the energy equation with the mass and momentum equations

$$\frac{\partial \alpha_k \rho_k}{\partial t} = 0 \quad \text{and} \quad \alpha_k \rho_k \frac{\partial u_k}{\partial t} = \pm \lambda (u_l - u_g)$$

we get

$$\alpha_k \rho_k \frac{\partial e_k}{\partial t} \pm \lambda u_k (u_l - u_g) = \pm \lambda V_i (u_l - u_g),$$

that is,

$$\frac{\partial e_k}{\partial t} = \pm (V_i - u_k) \frac{\partial u_k}{\partial t},$$

or also,

$$\frac{\partial e_k}{\partial t} = V_i \frac{\partial u_k}{\partial t} - \frac{\partial u_k^2/2}{\partial t}. \tag{41}$$

We make an approximate integration of this equation,

$$e_k = e_{k0} \pm \bar{V}_i (u_k - u_{k0}) - \tfrac{1}{2} \left(u_k^2 - u_{k0}^2 \right).$$

By estimating $\bar{V}_i$ as $\bar{V}_i = (V_i^n + V_i^{n+1})/2$ and $V_i^{n+1} = u_k$ we get

$$e_k = e_{k0} \pm \tfrac{1}{2} (u_k - u_{k0}) \left(V_i^n - u_{k0} \right). \tag{42}$$

After correction of the velocities and internal energies by Eqs. (40) and (42), respectively, the conservative vector can be rebuilt.

It finally remains to solve the last ODE problem, when the pressure relaxation coefficient tends to infinity.

Instantaneous Pressure Relaxation

Here we give details of the operator L_{PR} when μ tends to infinity. The assumption of instantaneous pressure relaxation is absolutely necessary for interface resolution. It is also necessary when the μ variable has not been determined physically or experimentally and

is unknown. The best estimate for this variable in such a case is to consider it infinite. Considering the dynamic compaction viscosity as infinite and looking at the solution at a finite time is identical to considering μ as finite and to looking at the steady state solution of the differential problem (43):

$$\frac{\partial U}{\partial t} = PR(U). \tag{43}$$

For the gas phase, we have

$$\begin{aligned}
\frac{\partial \alpha_g}{\partial t} &= \mu(P_g - P_l) \\
\frac{\partial \alpha_g \rho_g}{\partial t} &= 0 \\
\frac{\partial \alpha_g \rho_g u_g}{\partial t} &= 0 \\
\frac{\partial \alpha_g \rho_g E_g}{\partial t} &= -\mu P_i (P_g - P_l).
\end{aligned} \tag{44}$$

By combining the energy equation with the volume fraction equation we get

$$\frac{\partial \alpha_g \rho_g E_g}{\partial t} = -P_i \frac{\partial \alpha_g}{\partial t}.$$

We recover here a well-known result that is nothing else than the first law of thermodynamics for an isentropic transformation in a closed system. Integration of this equation yields

$$(\alpha_g \rho_g E_g)^* - (\alpha_g \rho_g E_g)^0 = - \int_{\alpha_g^0}^{\alpha_g^*} P_i \, d\alpha_g \tag{45}$$

and a similar result is obtained for the other phase:

$$(\alpha_l \rho_l E_l)^* - (\alpha_l \rho_l E_l)^0 = + \int_{\alpha_g^0}^{\alpha_g^*} P_i \, d\alpha_g.$$

The state with superscript 0 corresponds again to the state obtained after the previous integration steps : hyperbolic or relaxation. The state with superscript $*$ is the one we are looking for. So, we are looking for α_g^* such that the two pressures are equal: $P_g = P_l$. The procedure can be summarized as follows:

(a) Make an initial guess for α_g^*.
(b) Compute the integrals $(\alpha_g \rho_g E_g)^*$ and $(\alpha_l \rho_l E_l)^*$ by a suitable method.
(c) Compute the pressures P_g and P_l. Knowledge of $(\alpha_g \rho_g E_g)^*$ and $(\alpha_g \rho_g)$ that is a constant during the entire relaxation process allows easy computation of the total energy E_g^* and also of the internal energy e_g^*. Simultaneously, knowledge of α_g^* allows computation of ρ_g^*. Then, the pressure P_g^* is easily computed from the EOS: $P_g^* = P_g(\rho_g, e_g)$.
(d) Iterate this procedure until $P_g = P_l$.

This procedure is very accurate, but expensive when the integrals of step (b) need to be computed with a specific integrator. For nearly all test problems presented in Section 6, this is not necessary, and the approximate method that follows is sufficient.

Combination of mass, momentum, and energy equations yields

$$\frac{\partial e_g}{\partial t} = -P_i/\alpha_g \rho_g \frac{\partial \alpha_g}{\partial t}.$$ (46)

Approximate integration of this equation yields the result

$$e_g^* = e_g^0 - \bar{P}_i/(\alpha_g \rho_g)(\alpha_g^* - \alpha_g^0).$$ (47)

$\bar{P}_i$ represents the mean interfacial pressure between states $(\alpha_g^0, \rho_g^0, e_g^0)$ and $(\alpha_g, \rho_g, e_g)^*$. An equation similar to (47) is easily obtained for the liquid phase. So, the steady state solution of Eq. (43) now consists in finding the solution of

$$f(\alpha_g) = P_g(\rho_g, e_g) - P_l(\rho_l, e_l) = 0.$$

The pressures are given by their equations of state, with input $\rho_k = (\alpha_k \rho_k)^0/\alpha_k$ and $e_k = e_k^0 - \bar{P}_I/(\alpha_k \rho_k)^0(\alpha_k - \alpha_k^0)$. The mean interfacial pressure $\bar{P}_i$ is approximated by $\bar{P}_i = 0.5(P_i + P_i^0)$, where P_i^0 is computed at state $(\alpha_g^0, \rho_g^0, e_g^0)$ and P_i is estimated at (α_g, ρ_g, e_g) during the iterative procedure for solving $f(\alpha_g) = 0$.

6. TEST PROBLEMS

Test problems for multiphase flows (two velocities) are rather rare. We have selected three multiphase flow problems that will be presented at the end of this section. It is easier to find multifluid test problems (one velocity), with accurate reference solutions. The corresponding test problems are presented in order of increasing rate of difficulty for the algorithm. Each test problem is solved with the new numerical method, with the HLL Riemann solver, and is extended to second order as detailed previously. All computations are made with a CFL number of 0.8. They all use the approximate pressure relaxation procedure given by Eq. (47), except for the last test case, which uses the more accurate procedure given by Eq. (45).

6.1. Multifluid/Interface Test Problems (Instantaneous Pressure and Velocity Relaxation)

Water–Air Shock Tube

We consider a shock tube filled on the left side with high-pressure liquid water and on the right side with air. This test problem consists of a classical shock tube with two fluids and admits an exact solution. In this test problem, classical methods fail at the second time step. Each fluid is governed by the Stiffened gas equation of state (Godunov *et al.* [19]),

$$P = (\gamma - 1)\rho e - \gamma \pi,$$ (48)

where γ and π are constant parameters. The initial data are

$\rho_l = 1000 \text{ kg/m}^3$, $P_l = 10^9$ Pa, $u_l = 0$ m/s, $\gamma_l = 4.4$, $\pi_l = 6 \cdot 10^8$ Pa, $\alpha_l = 1 - \varepsilon$ ($\varepsilon = 10^{-8}$)

if $x < 0.7$;

$\rho_g = 50 \text{ kg/m}^3$, $P_g = 10^5$ Pa, $u_g = 0$ m/s, $\gamma_g = 1.4$, $\pi_g = 0$ Pa, $\alpha_g = 1 - \varepsilon$ otherwise.
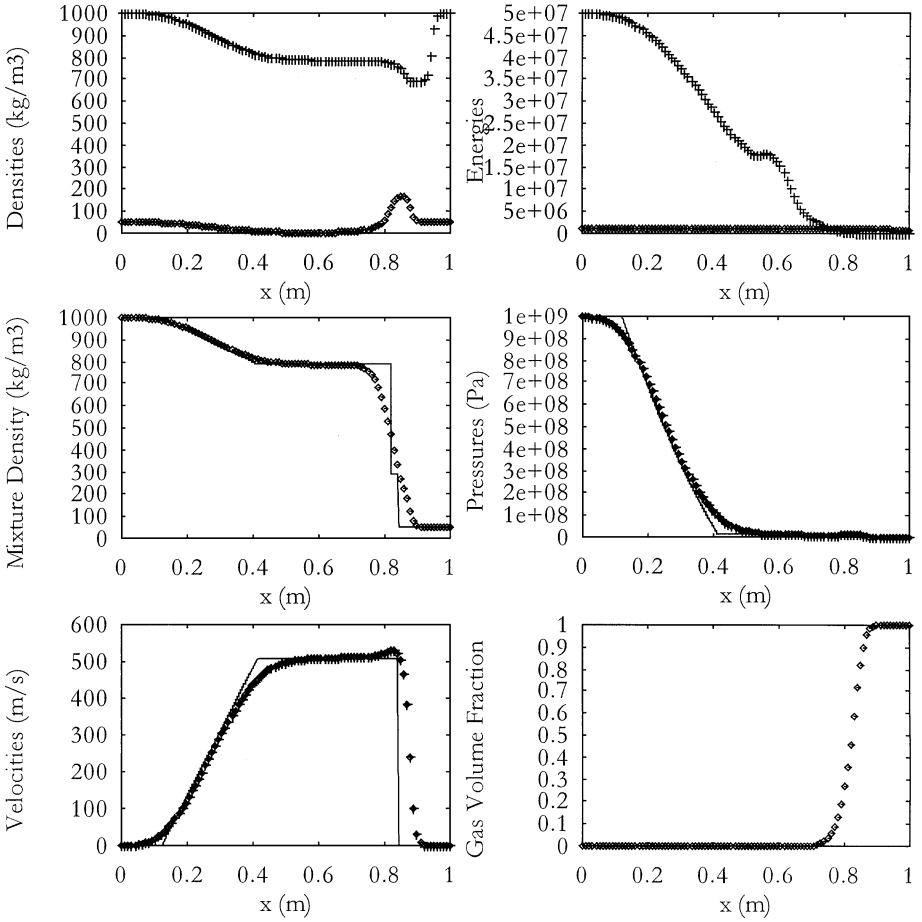
FIG. 6. Comparison between exact and numerical solutions in the water–air shock tube test case with 100 computational cells.

For a first run, we use a mesh with 100 cells. The corresponding results are shown in Fig. 6 at time 229 μs. In this test case, the right and left chambers contain nearly pure fluids: the volume fraction of gas in the water chamber is only 10^{-8} and inversely in the gas chamber. The phases densities and internal energies are not compared with the exact solution because no exact solution exists for the variables. But the mixture density, phases pressures, and velocities can be compared with the exact solution. The graphs showing the pressures and velocities show in fact three curves: two numerical curves and the exact solution. The two curves representing gas and liquid pressure and velocities are indiscernible. This is a result of the pressure and velocity relaxation procedures, which give an accurate relaxed state.

The lower curve on the internal energy graph corresponds to the liquid phase and the upper curve to the gaseous phase. The gas internal energy is particularly high in the high-pressure chamber because the gas density is low (and the pressure high). The density graph shows two curves. The upper curve corresponds to the liquid phase, and the lower curve to the gas phase. The shock wave propagating in the gas and the rarefaction wave in the liquid are clearly visible. In the liquid phase, some oscillations appear at the shock front. Instead of a density jump at the shock front in the liquid phase, there is a density decrease due to the pressure relaxation process. The liquid must have a density decrease in order to reach

the same pressure as that of the gas phase. The density oscillations at the liquid shock front have no influence since they are weighted by the liquid volume fraction, which is nearly zero in this zone.

Pressures, velocities, and mixture densities are compared with the exact solution represented by lines, while the numerical solution is represented by symbols. The mixture density is obtained by combination of the phase densities, which are summed and weighted by the volume fraction. The graph representing the mixture density shows an excessive numerical diffusion of the discontinuities. This is a result of the stiffness of this problem. The two materials, air and water, are very different in behavior and in EOS parameters, and the pressure ratio is excessively high (see the pressure graph). This situation for the liquid phase is close to a situation where the liquid should be connected to a vacuum. Also, the excessive numerical diffusion is a result of our approximate Riemann solver. It uses only two waves instead of seven, which for this practical application, because the sound speeds of the materials are very different, causes excessive smearing of the slowest waves. This can be remedied by following the method proposed by Gallouet and Masella [17]. To show mesh convergence of the results, the same computation is now made on a mesh involving 1000 cells. The results are shown in Fig. 7. It appears clear that the correct wave speeds are reproduced by the method, and that it converges to the correct solution.
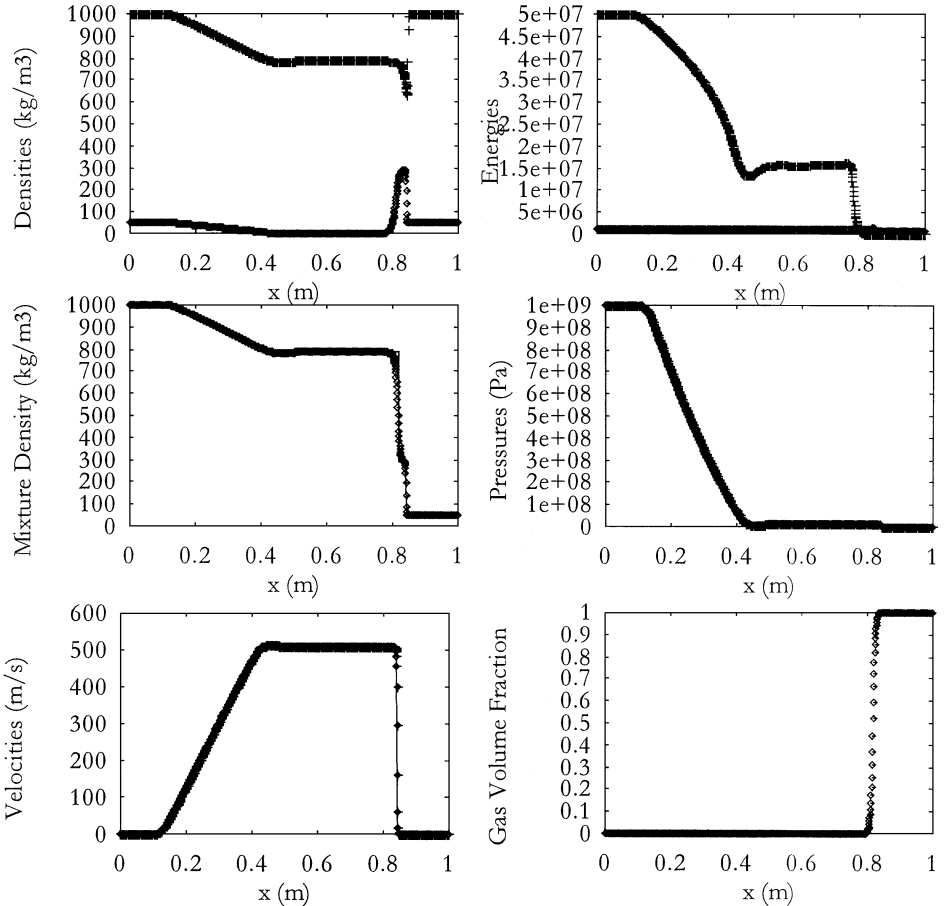

FIG. 7. Comparison between exact and numerical solutions in the water–air shock tube test case with 1000 computational cells.
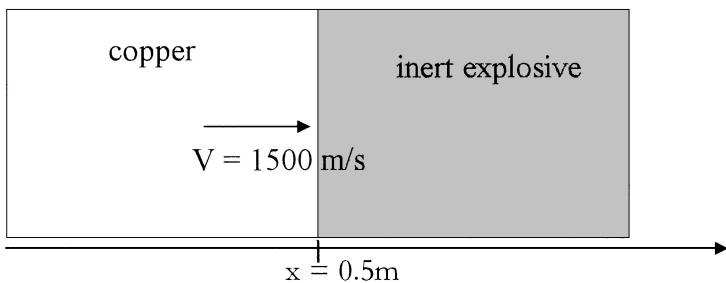
FIG. 8. Schematic representation of the impact of a copper plate on an inert explosive.

Real Material Interactions

In order to show that the method works correctly with complex equations of state, we have retained difficult test problems, representative of detonation physics. The first test problem involves two materials governed by the Cochran and Chan [9] equation of state. It is widely used to describe solids under high-pressure shock wave and is more accurate than the Stiffened gas EOS under these conditions. This EOS can be written in the Mie–Gruneisen form

$$P = P_k(\rho) + \rho\Gamma(e - e_k(\rho)), \qquad (49)$$

where P_k and e_k read

$$e_k(\rho) = -\frac{A_1}{\rho_0(1 - E_1)}\left[\left(\frac{\rho_0}{\rho}\right)^{1-E_1} - 1\right] + \frac{A_2}{\rho_0(1 - E_2)}\left[\left(\frac{\rho_0}{\rho}\right)^{1-E_2} - 1\right] - C_vT_0$$

$$(50)$$

$$P_k(\rho) = A_1\left(\frac{\rho_0}{\rho}\right)^{-E_1} - A_2\left(\frac{\rho_0}{\rho}\right)^{-E_2}.$$

This EOS has a limited domain of validity. When the density decreases slightly below the standard density ρ_0, the pressure becomes unrealistic (negative). So, it is important to have an accurate solution of the fluid properties at the interface. A more detailed presentation of the equations of state and their application is given in Saurel and Massoni [41]. The test problem considered here consists of the impact of a copper plate on a solid explosive considered as an inert material. The copper has an initial velocity of 1500 m/s, while the explosive is at rest (Fig. 8).

The two materials are under atmospheric conditions and their EOS parameters are summarized in Table I. The solution of this impact problem consists of a shock wave facing to

TABLE I
Material Properties for the Mie–Gruneisen EOS

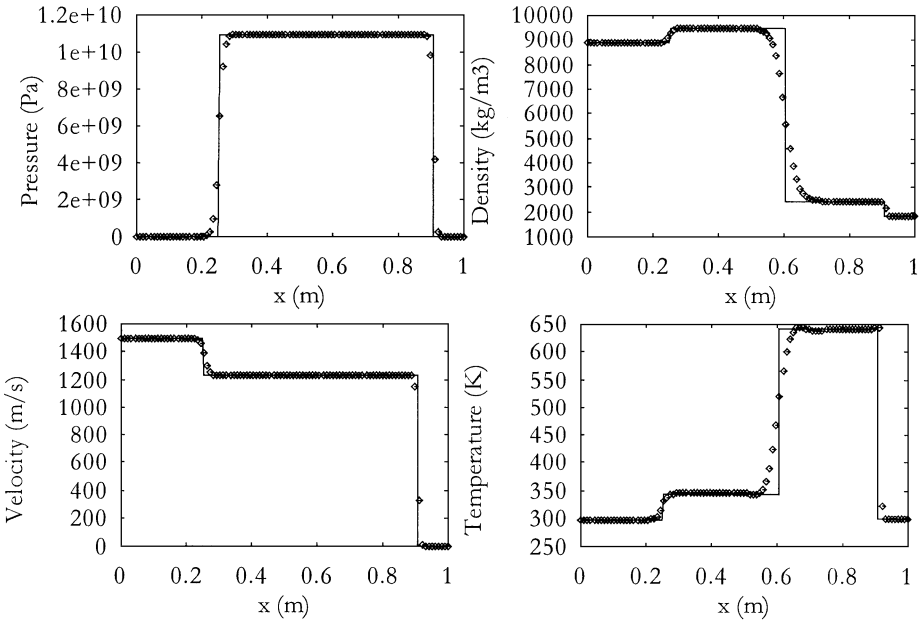|	Copper	Explosive
ρ_0 (kg/m^3)	8900	1840
Cv (J/kg · K)	393	1087
T_0	300	300
E_1	2.994	4.1
E_2	1.994	3.1
A_1 (Pa)	1.45667×10^{11}	1.2871×10^{10}
A_2 (Pa)	1.47751×10^{11}	1.34253×10^{10}
Γ	2	0.93

FIG. 9. Comparison between exact and numerical solutions of the impact problem. Computations were made over 100 cells.

the right and propagating in the inert explosive, and another shock wave facing to the left and propagating in the copper. Since the solution consists of two shock waves, classical Rankine–Hugoniot relations can be combined to provide the exact solution of this problem. The numerical solution is obtained again with the seven-equation model and the associated numerical method. Each fluid is considered as a mixture of two fluids that contains a very small percentage of one of the fluids, as for the water–air problem.

Comparison shown in Fig. 9 shows excellent agreement between the exact and numerical solutions. The results are shown at time 85 μs. For these computations, we used a mesh with only 100 cells. It is easily noticed that the various waves propagate at the correct velocity and that the numerical solution matches the exact one. It is also important to note that the temperature is correctly computed, also at the interface. This is a specificity of our method. To our knowledge, most other interface methods (Lagrangian, Eulerian, or Front Tracking) do not provide such accuracy for the temperature computation, except for a recent method proposed in Fedkiw *et al.* [15]. We also notice that the accuracy of the solution is better in this test case with only 100 cells than in the previous test case with the liquid–gas shock tube. The reason is that the density ratio between the two materials is lower than that in the previous case. More physically realistic applications of such impact problems are given in Massoni *et al.* [28].

We now consider a more difficult test problem involving two materials governed by two different equations of state, and again under drastic conditions as in detonation problems. We consider the interaction of gaseous detonation products with a copper plate (Fig. 10). Copper is governed by the Cochran and Chan EOS described previously, while the detonation products are governed by the most popular EOS for this type of fluid: the JWL EOS (Lee *et al.* [27]). It can again be written in the Mie–Gruneisen form (15), but the various functions
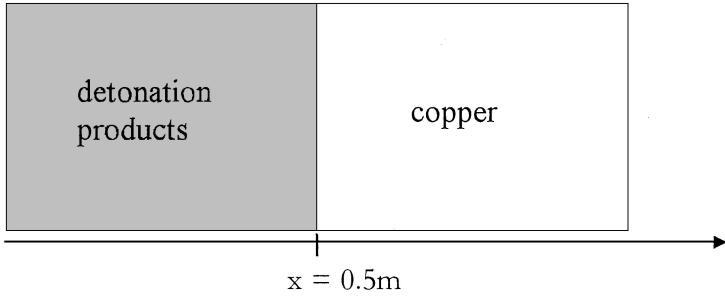
FIG. 10. A shock tube problem with explosive products and solid material.

are very different from those of the Cochran–Chan EOS. They are expressed as

$$e_k(\rho) = \frac{A}{\rho_0 R_1} \exp\left(-R_1 \frac{\rho_0}{\rho}\right) + \frac{B}{\rho_0 R_2} \exp\left(-R_2 \frac{\rho_0}{\rho}\right) + c_{ek}$$

$$P_k(\rho) = A \exp\left(-R_1 \frac{\rho_0}{\rho}\right) + B \exp\left(-R_2 \frac{\rho_0}{\rho}\right)$$

$$c_{ek} = -\frac{A}{\rho_0 R_1} \exp\left(-R_1 \frac{\rho_0}{\rho_{CJ}}\right) - \frac{B}{\rho_0 R_2} \exp\left(-R_2 \frac{\rho_0}{\rho_{CJ}}\right) - \frac{(P_{CJ} - P_{kg}(\rho_{CJ}))}{\rho_{CJ} \Gamma_g} + e_{CJ} \quad (51)$$

$$e_{CJ} = 0.5 \, P_{CJ} \left(\frac{1}{\rho_0} - \frac{1}{\rho_{CJ}}\right)$$

$$\rho_{CJ} = \frac{D_{CJ}^2 \rho_0^2}{D_{CJ}^2 \rho_0 - P_{CJ}}.$$

These functions require knowledge of the Chapman–Jouguet state (CJ). It can be deter-
mined with a thermochemical code like CHEETAH (Fried [16]), QUARTET (Bauer and
Heuzé [6]), QUERCY (Baudin [5]), etc. The JWL parameters necessary for the present com-
putations are summarized here: $A = 8.545 \; 10^{11}$ Pa, $B = 2.05 10^{10}$ Pa, $R_1 = 4.6$, $R_2 = 1.35$,
Cv $= 815$ J/(kg $\cdot$ K), $\Gamma = 0.25$, $P_{CJ} = 3710^9$ Pa, $D_{CJ} = 8800$ m/s, $T_{CJ} = 4040$ K, $\rho_0 = 1840$ kg/m^3. Initially, the copper is under atmospheric conditions and the detonation prod-
ucts are at the CJ state with regard to pressure, density, and internal energy and at zero
velocity. The solution of this test problem consists of an intense shock wave propagating
in the copper and a rarefaction wave facing to the left propagating in the gases. Due to the
complexity of the equations of state no exact solution is available for this test problem, but
it is possible to compute an accurate numerical solution with a front tracking code. Front
tracking methods solve the Euler equation in each of the two media with an appropriate
equation of state coupled with a specific scheme at the interface. The details of our front
tracking scheme are given in Saurel and Massoni [41]. The corresponding code has been
validated. So we can compare its prediction with the new method, in which we consider
each medium as a two-phase mixture with a negligible proportion of one of the fluids. The
results are shown in Fig. 11 at time 73 μs. The front tracking results are shown by lines,
while the results obtained with the multiphase model and method are shown by symbols.
Agreement is again excellent. The advantage of the new method with the multifluid model
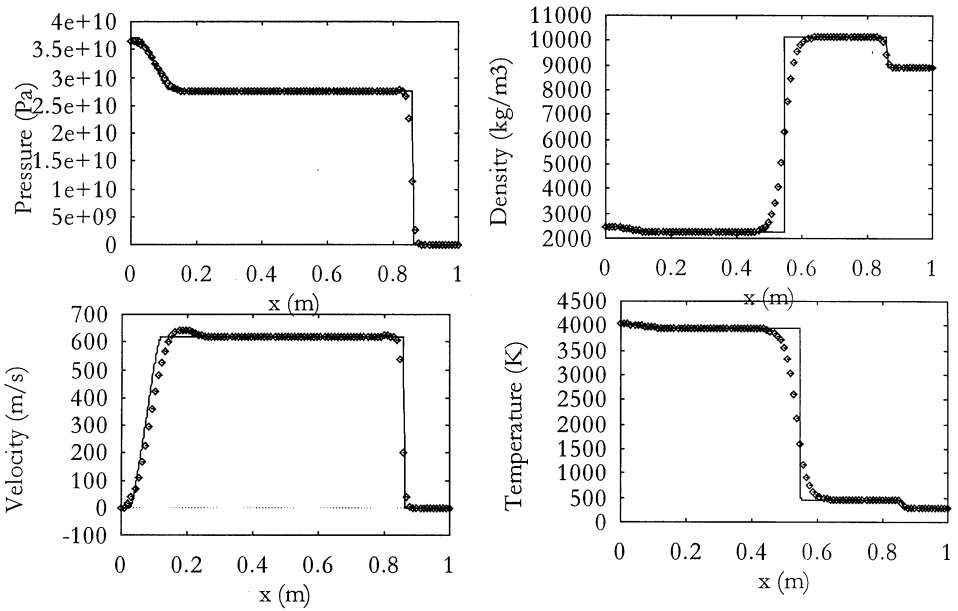compared to the front tracking method with the Euler equations is that extension to an

FIG. 11. Comparison between the interface tracking solution and the new method used in the detonation shock tube problem. Computations were made over 100 cells.

arbitrary number of interfaces in 2D or 3D is not difficult, while extension to the front tracking method in more than 1D is delicate (Cocchi and Saurel [8]).

6.1. Multiphase Test Problems (Two Velocities)

For the following test problems, the pressure relaxation procedure is used, but not the velocity relaxation procedure, so each phase possesses its own velocity. The same system with seven equations is solved, with the same numerical method.

Water Faucet Problem

We now consider another test problem, in which the behavior of the two fluids is incompressible, and we try to model them as compressible with the previous model and method. Of course our model is rather complex for such a problem and it is possible to build a simpler model for such an application (Toumi and Kumbaro [49]), but our goal is to show that the model is able to work also on incompressible flows. The water faucet problem consists of a vertical tube 12 m in length. The top has a fixed liquid velocity (10 m/s) and a liquid volume fraction of 0.8. The bottom of the tube is open to atmospheric conditions. The problem is schematized in Fig. 12. Initially, the tube is filled with a uniform column of liquid water at a velocity of 10 m/s surrounded by a gas at a volume fraction of 0.2. The gas inlet velocity is zero, so it is necessary to consider two distinct velocities. Therefore, the multiphase model with two velocities is used. From these initial conditions, gravity effects are solved and provoke a lengthening of the liquid jet. The various events are represented in Fig. 12. The exact solution for this problem is available (Coquel *et al.* [10]) and is represented by bold lines in Fig. 13. The numerical solution is represented by thin lines. The gas and liquid are treated as compressible fluids with the same parameters and equations of state as those for the liquid–gas shock tube test problem.
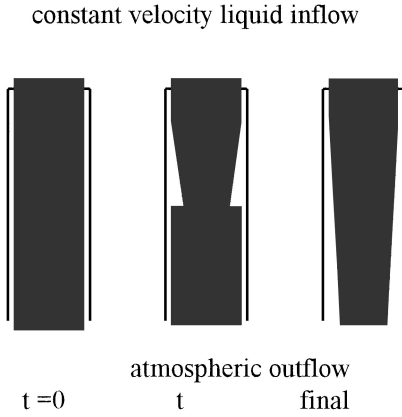
constant velocity liquid inflow

atmospheric outflow

t =0   t   final

FIG. 12.   Schematic representation of the water faucet problem.

The numerical solution shows good agreement with the exact one, even though the conditions of this test problem are far from the range of application of our model. The excessive numerical diffusion of the volume fraction wave is due to the poor accuracy of our Riemann solver and to the low Mach number conditions of this test problem. The HLL Riemann solver has been used here. It estimates a mean state between the maximum speed right-facing wave and minimum speed left-facing wave. Here these waves are acoustic waves, and their velocity is several orders of magnitude larger than that of the liquid velocity. The gas volume fraction propagates at a velocity close to that of the liquid one. So the computation of the variables associated with low velocity cannot be very accurate with such a solver. Also, the low Mach number conditions are restrictive for our method, restricted by the CFL condition. An implicit scheme with appropriate preconditioners should be better (see Guillard and Viozat [20]).

Rogue Test Problem

Consider a long vertical shock tube filled with air. In a given section of the driver chamber, a finite thickness dense bed of solid particles has been settled. When the shock wave
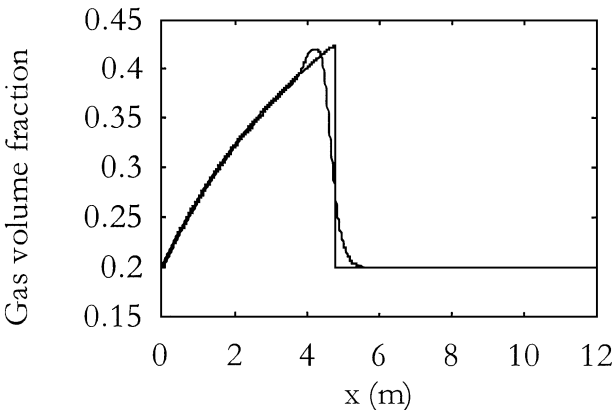

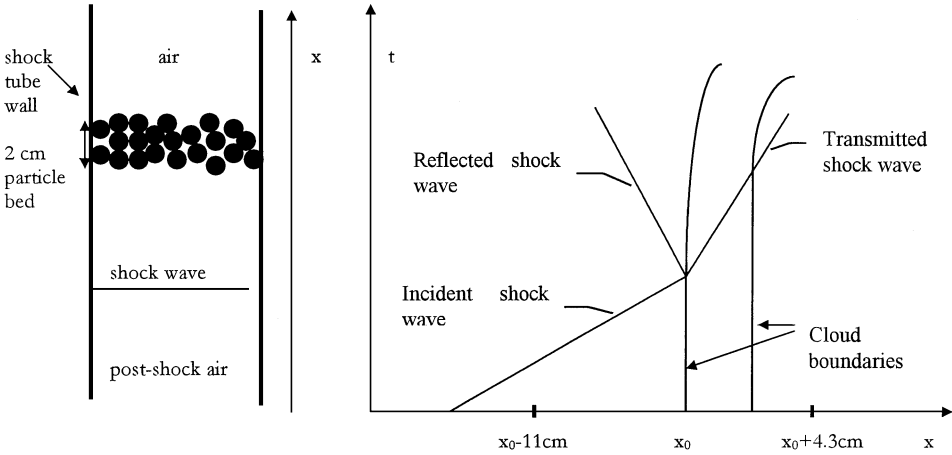**FIG. 13.**   Gas volume fraction at time 0.4 s (exact solution, bold lines).

FIG. 14.   Schematic representation of the Rogue two-phase shock tube and corresponding wave pattern.

propagates through the bed, pressure and drag effects set the particles into motion. Simultaneously, the incident shock wave diffracts in a transmitted shock wave propagating into the particle bed, and a reflected shock wave propagating backward. During the propagation of the transmitted shock wave, drag effects and the effect due to the volume occupied by the particles weaken the shock wave. During the same time period, particles are set into motion and the bed starts from a dense configuration and tends progressively to a dilute one. The various waves are represented in Fig. 14. Two pressure gauges are located on the shock tube wall at 4.3 cm upper and 11 cm lower from the initial location of the particle bed. They record the gas pressure evolution versus time.

This test problem is a rather complicated one for which no analytical solution is available. But careful experimental results have been obtained for it and can serve as reference for the computations. The main difficulty of the computations is that two interfaces between a pure gas flow and a two-phase gas-particle flow are present. Previous simulations of this test problem (Rogue [32], Rogue *et al.* [33]) have shown weak accuracy in the computation of the dilution effects in the particle cloud and pressure records. We now test our model and method on this problem.

Under the weak shock wave propagation, the behavior of the solid particles is incompressible. But we model them as weakly compressible particles, in order to have a well-posed mathematical model. Under these pressure conditions, we can assume that the solid particles are governed by the Stiffened gas equation of state with the parameters of liquid water (given above). To model the shock wave interaction with particles we need a drag force. This force was not considered in the previous test problem, but it now plays a major role. Heat exchanges and intergranular stress effects have been estimated previously: they have a negligible influence. The drag force is expressed as

$$F_d = \frac{3}{4} C_d \frac{\rho_g}{d_p} (1 - \alpha_g) |u_g - u_p| (u_g - u_p). \tag{52}$$

The data necessary for the following simulation are summarized in Table II.

In Fig. 15 we have reported the experimental and numerical pressure signals recorded by the pressure gauges. The lower pressure gauge records the incident shock wave at a pressure of about 1.8 atm. About 0.7 ms later, it records the passage of the reflected shock wave at

TABLE II
Parameters for the Rogue Test Problem

Air preshock density	$1.2 \ \text{kg/m}^3$
Incident shock Mach number	1.3
Particle density	$1050 \ \text{kg/m}^3$ (nylon)
Particle diameter	2 mm
Particle bed thickness	2 cm
Initial gas volume fraction in the bed	0.35
Drag coefficient (C_d)	0.6

about 3 atm. At about the same time, the upper pressure gauge records the passage of the transmitted shock wave at about 1.2 atm. This shock wave has been attenuated because of variation of the cross section in the particle bed and momentum exchanges. From this time, the gas continues its flow inside the particle bed and exchanges momentum with it. The particle bed separates a high pressure zone at about 3 atm from a low pressure zone at about 1.2 atm. Motion of the particle bed and penetration of gases in it tend to equilibrate these pressures. It is why the lower pressure gauge signal decreases and the upper one increases. At time 2.2 ms, the cloud of solid particles reaches the upper pressure gauge. From here to about 3.5 ms, the gauge records the pressure inside the fluidized bed.

Numerical simulation produces reliable results of these phenomena. Some differences are visible between experiment and simulation, which are possibly due to boundary layer effects and uncertainty in the drag coefficient. But improvement in accuracy is good compared to that attained in previous simulations: Eulerian and Lagrangian models. This gain in accuracy is due to the mathematically well-posed model and to the treatment on the interfaces between
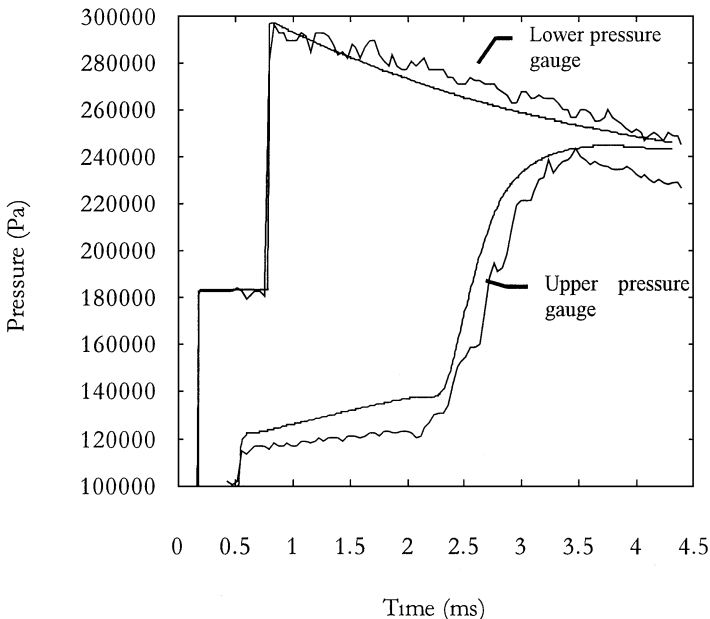

FIG. 15. Comparison of the experimental pressure records and the numerical pressure signal in the Rogue test problem.
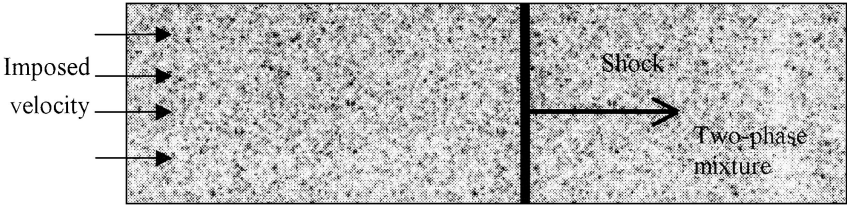
FIG. 16. Schematic representation of the two-phase shock wave problem.

pure gas and two-phase mixtures. Also, we can again see that modeling of solid particles as compressible media is not a severe restriction.

Mixture Hugoniot Test Problem

We now evaluate the model and method capabilities for computation of shock waves in two-phase mixtures with a test problem involving very strong shock waves. The two-phase system does not admit classical Rankine–Hugoniot relations because non-conservative and relaxation terms are present in the equations. But it is possible to solve these equations in an unsteady regime with the proposed numerical method, and to examine the two-phase shock wave behavior. To do this, we simulate impact situations over two-phase mixtures by considering the impact as a boundary condition (Fig. 16).

In order to evaluate computed results, we need reference solutions. Since classical Rankine–Hugoniot conditions do not exist for the two-phase system, it is not possible to determine the exact solution. But it is possible to find specific situations where experimental results are available. Indeed, for many pure liquids and solids, the relation between shock velocity and material velocity is a linear relation, intrinsically characteristic of the material, and experimentally determined,

$$U_s = c_0 + sU_p, \tag{53}$$

where c_0 is the material sound speed under atmospheric conditions, U_s the shock velocity, U_p the material velocity, and s a dimensionless constant. This relation is valid for a shock wave propagating in solid or liquid materials, under atmospheric conditions, and initially at rest. A large database is given in Marsh [29]. When the experimental relation (53) is known, it is possible to derive an equation of state for the material. Nearly all condensed phase equations of state are based on this relation. The simplest EOS is the Stiffened gas EOS, given by relation (48).

What is now particularly interesting is that relation (53) is also available for some metal alloys. Under strong shock waves, these alloys may be considered as two fluid mixtures. For example, brass under strong shock wave may be considered as a two-phase mixture composed of copper and zinc. Since relation (53) is known for both copper and zinc, we are able to determine the Stiffened gas EOS parameters for each material, and compute the associated two-phase flow with the seven-equation model. Simultaneously, relation (53) is also known for brass and will be our reference solution.

For a metal alloy, the two-phase mixture is made of very fine particles perfectly mixed at the macroscopic scale. Due to the small particle size and large "viscosity" of the solid materials, the best estimates for the relaxation parameters (pressure and velocity) is to consider them infinite. This corresponds to a situation where the two pressures and velocities relax instantaneously after wave propagation toward common pressure and velocity.

In this test problem, we compare two theoretical approaches. The first one is of course based on the two-phase flow equations. It involves solution of the seven-equation system closed by the two EOS for each pure material. The second approach consists in the solution of the Euler equations with a mixture equation of state. Mixture equations of state are based on several assumptions:

—The mixture is under pressure and velocity equilibrium;
—all components of the mixture possess the same density or the same temperature or any equilibrium assumption for one of the other thermodynamic functions.

The first assumption is reasonable and realistic for such flow conditions. The second assumption is arbitrary and is not supported by any experimental or theoretical evidence. In spite of this uncertainty, mixture EOS are coupled to the Euler equations for the computation of detonation waves in solid energetic materials in nearly all CFD codes. An example is given in Saurel and Massoni [41].

The simplest way to build mixture EOS for solid mixtures is obtained on the basis of the mixture Stiffened gas EOS. If each pure fluid is governed by relation (48) and under the assumption that the mixture fulfills the same relation, the mixture EOS reads

$$P = (\Gamma - 1)\rho e - \Gamma \Pi,$$

where

$$\Gamma = 1 + \frac{1}{\frac{\alpha_1}{\gamma_1 - 1} + \frac{\alpha_2}{\gamma_2 - 1}} \quad \text{and} \quad \Pi = \frac{\Gamma - 1}{\Gamma}\left(\alpha_1 \frac{\gamma_1 \pi_1}{\gamma_1 - 1} + \alpha_2 \frac{\gamma_2 \pi_2}{\gamma_2 - 1}\right).$$

This method for mixture EOS is detailed in Massoni *et al.* [28]. It has also been used by Shyue [44] for the computation of interface variables in multifluid flows. We consider two metallic alloys for which relation (53) is available in Marsh [29]. The data for pure components are also available in the same reference. They are summarized in Tables III and IV.

With the two-phase code we compute several unsteady impact problems, by varying the velocity boundary condition, and we note the ratio of the shock velocity and the impact (material) velocity. We obtain the results shown in Fig. 17. The first graph is related to brass (Cu/Zn alloy), with an initial zinc volume fraction of 0.29. The second graph is related to the uranium/rhodium alloy with an initial rhodium volume fraction of 0.265. The last graph corresponds to an epoxy/spinel mixture, with an initial epoxy volume fraction of 0.595.

In Fig. 17, we have also represented the solution obtained with classical Rankine–Hugoniot relations from the Euler system, coupled with the mixture EOS. We notice

TABLE III
Stiffened Gas EOS Parameters for Pure Materials

	Density (kg/m³)	c_0 (m/s)	γ	π (10^9 Pa)
Copper	8,924	3910	4.22	32.4
Epoxy	1,185	2823	2.94	3.2
Rhodium	12,429	4790	3.61	79.0
Spinel	3,622	7954	1.62	141.0
Uranium	18,930	2510	3.52	33.9
Zinc	7,139	3030	4.17	15.7

TABLE IV
Stiffened Gas EOS Parameters for Selected Alloys

	Density (kg/m³)	c_0 (m/s)	γ	π (10^9 Pa)
Brass (Cu/Zn)	8,413	3520	4.32	24.1
Epoxy/Spinel	2,171	3090	3.47	5.98
Uranium/Rhodium	17,204	2740	3.53	36.6

excellent agreement for all test problems between the experimental data and two-phase results. The mixture EOS coupled with the Euler equations provides acceptable accuracy for the second mixture, but catastrophic results regarding the last one. The poor agreement between mixture EOS and experimental results is related to the assumption of density equilibrium, used for building this EOS. It is also important to note that, for the last test case, the Stiffened gas EOS parameters associated with the alloy obtained from the experimental data are not included in the range of the two other materials (epoxy and spinel). The spinel and epoxy γ are respectively 1.62 and 2.94 while the mixture γ is 3.47. The mixture Γ detailed previously cannot have such a behavior.

Some differences between the two-phase and experimental results are noticeable. Of course, these differences are minor compared to those associated with the mixture EOS. These differences between experimental results and the two-phase model may have several sources:
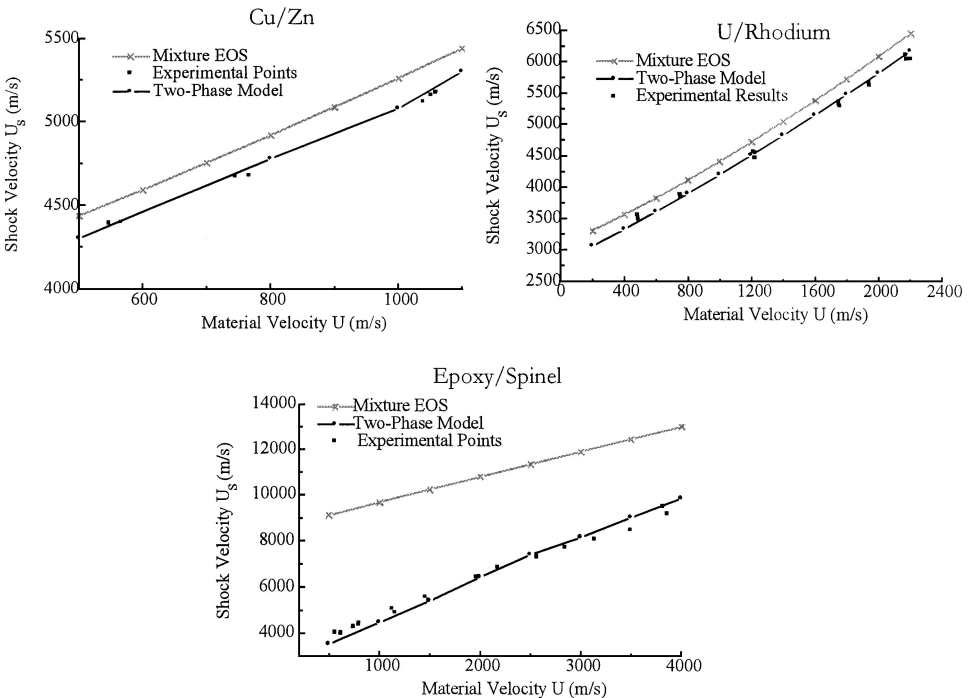

FIG. 17. Hugoniot curves of selected alloys. Comparison between experimental and theoretical curves obtained with Euler equations and mixture EOS and two-phase flow model with pure material EOS.

—These tests involve very high pressures (of the order of one million atmospheres).

—The experimental uncertainty is not negligible at these pressures.

—The discretisation formulae for non-conservative terms have been developed for a situation where pressure and velocity are uniform. A strong shock wave does not fulfill these conditions at all, but we discuss this further below.

—The pressure relaxation process in a solid may not be hydrodynamic. At the microscopic scale (grain scale), some plasticity or viscosity effects may intervene. In such a case, the pressure equilibrium is not obtained when $P_1 = P_2$, but with another relation like $P_1 = P_2 + P_y$, where the pressure P_y represents the effects related to plasticity.

In spite of these uncertainties, agreement is excellent, especially compared to predictions of the mixture EOS. It is also very interesting to explore the reasons for the discrepancies of the mixture EOS compared to those of the two-phase approach. An analysis of the two-phase flow variables will give us some indications (Fig. 18). We examine here the first alloy, composed of copper and zinc.

Pressure, volume fraction, and phase internal energies and densities are shown in Fig. 18 at three successive instants in the two-phase column. The shock wave propagation is clearly visible. This wave looks like a classical discontinuity. We can also notice that the two pressures are perfectly equilibrated, because each curve is the exact superposition of the zinc and copper pressures. On the curves related to the other flow variables, we can notice another wave or discontinuity propagating at a lower velocity. This wave propagates like a contact discontinuity, at the local flow velocity, and has no physical reality. It is related to the numerical treatment of the piston boundary condition. This problem with the Euler equations is well known. It is noticeable when a large piston velocity is used at the boundary. This problem is related to temporal convergence inaccuracies during the shock wave building at the boundary. This problem is still unsolved, even for the Euler equations. Recently, Fedkiw
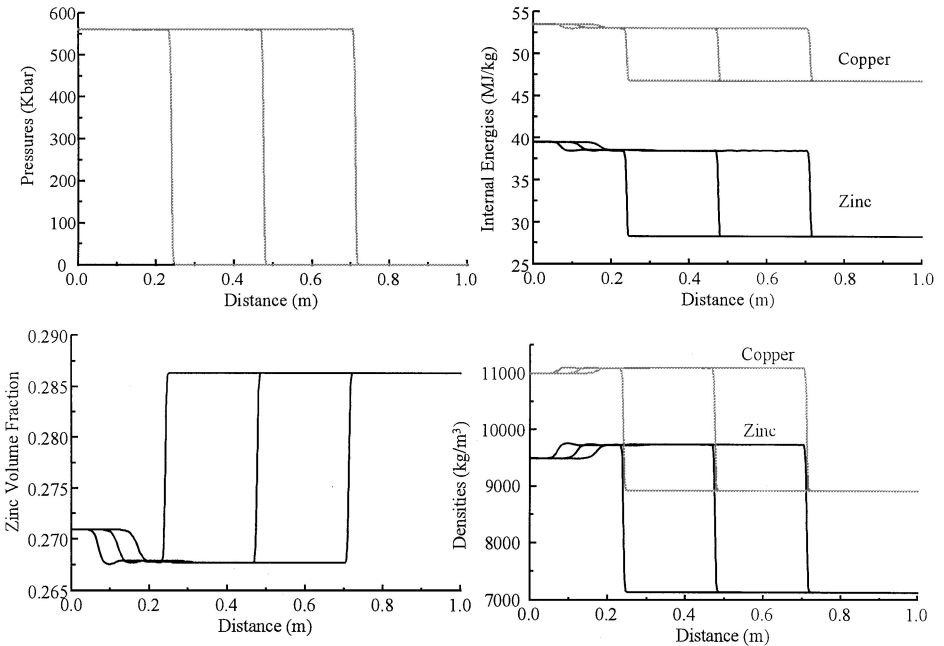

FIG. 18.   Two-phase flow variables for the Cu/Zn alloy under shock impact at 1200 m/s.

et al. [14] proposed a way to reduce or eliminate this problem on the basis of thermodynamic considerations, which we do not enter into here. This wave has no influence on the shock wave dynamics. The most interesting result for our problem is related to the volume fraction evolution. A strong variation of the volume fraction is clearly visible across the shock wave. This variation is due to the pressure relaxation process. After shock wave propagation, each of the two materials has its own pressure. Then the volume fraction evolves progressively inside the shock numerical diffusion zone, implying variations of the internal energies and densities of the two materials so that the two pressures are equal. The two materials have different compressibilities, and the more compressible material will be compressed while the other will be expanded. So, the volume fraction evolves inside the numerical shock wave. This volume fraction variation is responsible for correct computation of pressure. When the mixture EOS is used, the volume fraction is constant and equal to the initial volume fraction of the components of the two-phase mixture. Indeed, no evolution equation is available for the volume fraction equation and no pressure differential can be computed. It is unrealistic from a physical point of view for the volume fraction to be constant across a shock wave or any pressure wave. So, it is not surprising that inaccurate solutions are obtained when mixture EOS is coupled to the Euler system for multiphase mixture. These errors are not really noticeable in the uranium/rhodium test problem because the EOS parameters are not appreciably different and also because the densities after shock wave propagation are relatively close. For the epoxy/spinel test problem, the densities are always very different and there are many more differences regarding the EOS parameters for this test problem than for the previous test problems.

A last remark regarding numerical discretisation is necessary. The volume fraction equation (non-conservative equation) implies that the volume fraction propagates at the mean interfacial velocity (V_i), when the relaxation terms are omitted. The numerical scheme we have proposed gives a numerical approximation of this equation that propagates the volume fraction at the relaxed velocity, corrected by viscosity terms coming from the discretisation of the convective fluxes under the constraint "uniform pressure and velocity." When relaxation terms are omitted in this equation, this variable must have no variation across the shock wave. The discretisation scheme propagates this variable without variation across the shock front, which propagates at a very different velocity. So, the relaxation term $\mu \Delta P$ is responsible for the volume fraction variations across the shock front, as seems realistic from a physical point of view.

Cavitation Test Problem

Consider a tube filled with water and imagine that the left part of this tube is set in motion to the left, and the right part is set in motion in the opposite direction. The situation is represented in Fig. 19. In such a situation, pressure, density, and internal energy decrease across the rarefaction waves so that the velocity reaches zero at the center of the domain. The pressure decreases until it reaches the saturation pressure at the local temperature. When the saturation pressure is reached, mass transfer appears and part of the liquid becomes gas, and the flow becomes a two-phase mixture.

When this type of problem is solved with Euler equations, with a single-fluid approach and an appropriate equation of state for the liquid (the Stiffened gas EOS, for example), the pressure becomes rapidly completely wrong (i.e., negative). The EOS is written $P = (\gamma - 1)\rho e - \gamma \pi$. Across the rarefaction waves, density and internal energy decrease while the corrective pressure $\gamma \pi$ remains constant, and so the pressure becomes negative.
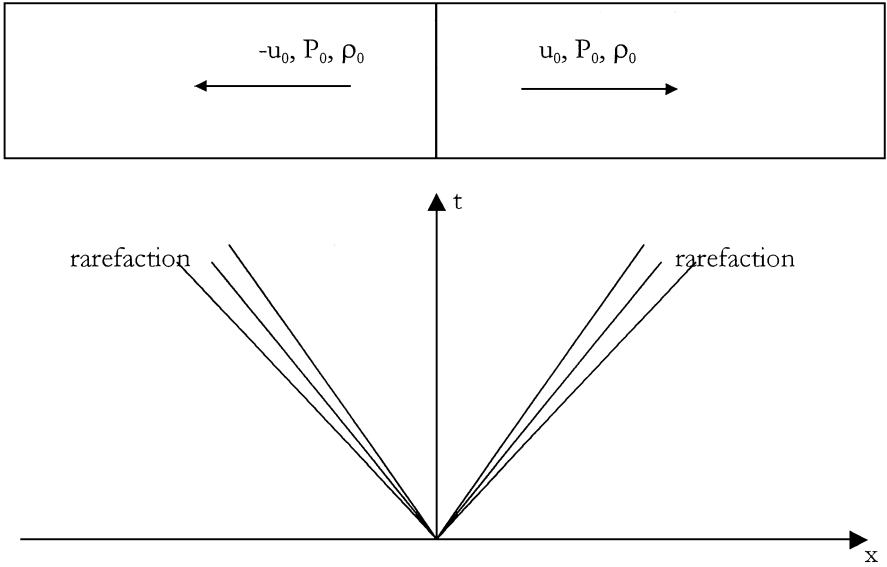
FIG. 19.   Schematic representation of a cavitation tube and associated rarefaction waves.

This is of course unrealistic. The reason is that the Stiffened gas EOS is no longer valid when the pressure becomes sub-atmospheric, because the liquid transforms into gas, and the gas does not have the same EOS, nor the same behavior.

There are two ways to solve this problem. The first is to build an EOS that is valid for the liquid phase, the two-phase mixture, and the gas phase. Such an approach is given by Saurel *et al.* [43]. But as usual in building mixture EOS, there are assumptions about the thermodynamics of the mixture—for instance, the assumption of temperature equilibrium or the assumption of thermochemical mixture equilibrium. For the present application, the assumption of temperature equilibrium between phases is not prejudicial, because the gas phase appears as a result of mass transfer, and mass transfer occurs at constant temperature. But, in the general case, there are situations for which this procedure can lead to unrealistic computations.

The second way to solve the problem is to use our non-equilibrium two-phase flow model. With this model, each phase possesses its own EOS and proper behavior. We propose to solve the test problem represented in Fig. 19 by the seven-equation model. The liquid phase will be governed by the Stiffened gas EOS, and the gas phase by the ideal gas EOS. Since mass transfer terms are not present in these equations, and because it is difficult to determine a finite rate model for mass transfer due to a pressure drop, we consider a simplified problem, in which initially the liquid column contains 1% gas by volume. From this initial situation, with the gas and liquid at atmospheric pressure, we set into motion the right part of the tube at 100 m/s, and the left part at -100 m/s.

The seven-equation model is solved on a mesh with 100 cells, with instantaneous pressure and velocity relaxation. Here we use the "exact" pressure relaxation method defined by Eq. (45). The results are shown in Fig. 20 and the various curves are separated by a time interval of 0.5 ms. The density graph shows the liquid and gas evolutions. The liquid density decreases slightly but remains closed to the initial one. The liquid remains liquid at a positive pressure. The gas density decreases across the rarefaction waves and decreases
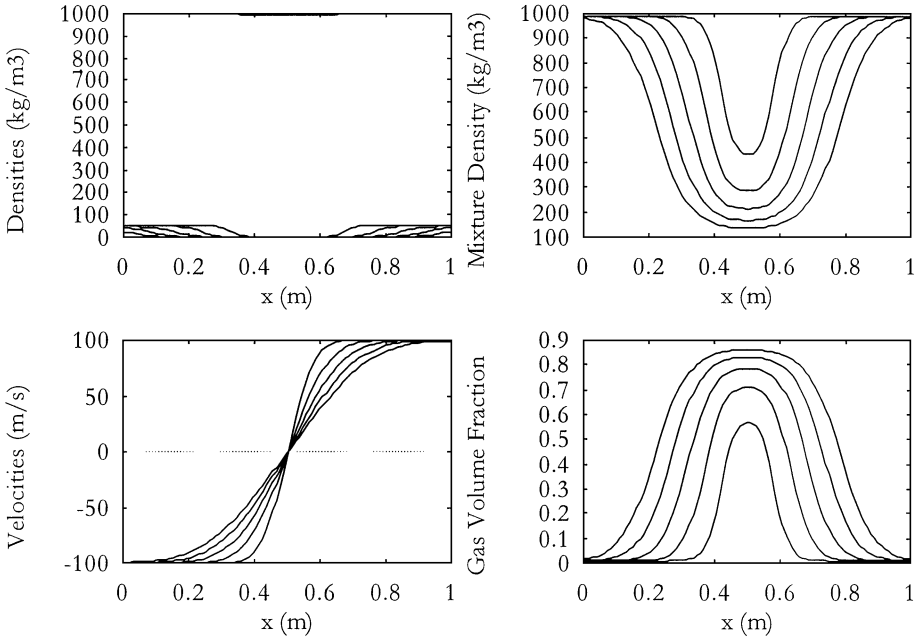
FIG. 20. Profiles of two-phase variables at times 0.5, 1, 1.5, 2, and 2.5 ms for the cavitation test problem.

again due to the pressure relaxation process. The gas density at the center of the tube is very low. The pressure relaxation process causes the gas volume fraction to increase. So, the mixture density decreases, as expected, and the velocity profile tends to the expected solution. It can also be noticed that the increase in gas volume fraction tends to create two interfaces that propagate to the right and to the left. These interfaces are two-phase ones. It can be concluded that, even starting from a situation in which interfaces are not present, the procedure is capable of dynamically creating interfaces. This feature can have important applications for specific problems and is a specific feature of this method.

7. CONCLUSIONS

An efficient model and a solution method have been proposed for the simulation of compressible multiphase and multifluid flows. The proposed model is hyperbolic, and the solution method is able to solve non-conservative terms in the equations and a non-conservative volume fraction equation. The model applies to pure fluids and to mixtures. The same numerical algorithm applies at each mesh point. It is able to deal with strong shock waves and complex equations of state, and to work on flows where one of the phases has an incompressible behavior. The success of this approach is due to three key points:

—building of hyperbolic models for compressible fluid mixtures,
—accurate solution of non-conservative terms and equations,
—relaxation procedure for pressures (and if necessary for velocities).

The model is hyperbolic because pressure equilibrium is not assumed in the formulation but is assumed only after the pressure relaxation step when necessary.

We plan to extend the method to chemically reacting flows, to flows with mass transfer, and to multi-dimensions. A simple way to do the last extension is given in Saurel and

Abgrall [40]. Extension of this method to unstructured meshes is under study. The method can be improved by increasing the accuracy of the Riemann solver and also by developing an implicit version for low Mach number flows.

ACKNOWLEDGMENT

REFERENCES

1. R. Abgrall, Generalization of the Roe scheme for the computation of a mixture of perfect gases, *Rech. Aérospat.* **6** (Dec. 1988).

2. R. Abgrall, How to prevent pressure oscillations in multicomponent flow calculations: A quasi conservative approach, *J. Comput. Phys.* **125**, 150–160 (1996).

3. M. R. Baer and J. W. Nunziato, A two-phase mixture theory for the deflagration-to-detonation transition (DDT) in reactive granular materials, *Int. J. Multiphase Flow* **12**, No. 6, 861–889 (1986).

4. M. R. Baer, A numerical study of shock wave reflections on low density foam, *Shock Waves* **2**, 121–124 (1992).

5. G. Baudin, Quercy, un programme de calcul thermochimique rapide pour évaluer l'état de Chapman-Jouguet et d'isentrope des explosifs condensés, Note Technique T92-36, Centre d'Etudes de Gramat (1992).

6. P. Bauer and O. Heuzé, A simple method for the calculation of detonation properties of CHNO explosives, in *Proceedings, International Symposium on High Dynamic Pressures, La Grande Motte, France, 1989*, pp. 225–232.

7. P. B. Butler, M. F. Lambeck, and H. Krier, Modeling of shock development and transition to detonation initiated by burning in porous propellant beds. *Combust. Flame* **46**, 75–93 (1982).

8. J. P. Cocchi and R. Saurel, A Riemann problem based method for compressible multifluid flows, *J. Comput. Phys.* **137**, 265–298 (1997).

9. G. Cochran and J. Chan, Shock initiation and detonation models in one and two dimensions, Lawrence Livermore National Laboratory Report (1979).

10. F. Coquel, K. El Amine, E. Godlewski, B. Perthame, and P. Rascle, A numerical method using upwind schemes for the resolution of two-phase flows, *J. Comput. Phys.* **136**, 272–288 (1997).

11. S. F. Davis, Simplified second order Godunov type methods, *SIAM J. Sci. Statist. Comput.* **9**, No 3, 445–473 (1988).

12. J. M. Delhaye and J. A. Bouré, General equations and two-phase flow modeling, in *Handbook of Multiphase Systems*, edited by G. Hestroni (Hemisphere, New York, 1982), Vol. 1, pp. 36–95.

13. D. A. Drew, Mathematical modeling of two-phase flows, *Annu. Rev. Fluid Mech.* **15**, 261–291 (1983).

14. R. P. Fedkiw, A. Marquina, and B. Merriman, An isobaric fix for the overheating problem in multimaterial compressible flows, UCLA Report (1998).

15. R. P. Fedkiw, B. Merriman, and S. Osher, Simplified upwind discretisation of systems of hyperbolic conservation laws containing advection equations, with applications to compressible flows of multiphase, chemically reacting and explosive materials, UCLA Report (1998).

16. E. Fried, CHEETAH 1.39 User's Manual, Energetic Material Center, Lawrence Livermore National Laboratory, UCRL-MA-117541, Rev.3 (1996).

17. T. Gallouet and J. M. Masella, Un schéma de Godunov approché, *C.R. Acad. Sci. Paris Sér. I* **323**, 77–84 (1996).

18. S. K. Godunov, A finite difference method for the numerical computation of discontinuous solutions of the equations of fluid dynamics, *Mat. Sb.* **47**, 357–393 (1959).

19. S. K. Godunov, A. Zabrodine, M. Ivanov, A. Kraiko, and G. Prokopov, *Résolution numérique des problèmes multidimensionnels de la dynamique des gaz* (Editions Mir, Moscow, 1979).

20. H. Guillard and C. Viozat, On the behavior of upwind schemes in the low Mach number limit, *Comput. & Fluids* **28**, 63–86, in press.

21. J. F. Haas, *Interaction of a Weak Shock Wave and Discrete Gas Inhomogeneities*, Ph.D. thesis, California Institute of Technology, Pasadena (1984).

22. J. F. Haas and B. Sturtevant, Interaction of a weak shock wave with cylindrical and spherical gas inhomogeneities. *J. Fluid Mech.* **181**, 41–76 (1987).

23. A. Harten, P. D. Lax, and B. van Leer, On upstream differencing and Godunov type schemes for hyperbolic conservation laws, *SIAM Rev.* **25**, No. 1, 33–61 (1983).

24. F. Harlow and A. Amsden, Fluid dynamics, LANL Monograph LA-4700 (1971).

25. O. Heuzé, Mémoire d'habilitation à diriger des recherches, Université d'Orléans (1997).

26. S. Karni, Multicomponent flow calculations by a consistent primitive algorithm, *J. Comput. Phys.* **112**, 31–43 (1994).

27. E. L. Lee, H. C. Horning, and J. W. Kury, Adiabatic expansion of high explosives detonation products, Lawrence Radiation Lab., University of California, Livermore, TID 4500-UCRL 50422 (1968).

28. J. Massoni, R. Saurel, G. Demol, and G. Baudin, A Mechanistic model for shock to detonation transition in solid energetic materials, *Phys. Fluids*, in press.

29. S. P. Marsh, *LASL Shock Hugoniot Data* (Univ. of California Press, Berkeley, 1980).

30. J. M. Powers, D. S. Stewart, and H. Krier, Theory of two-phase detonation. Part I. Modeling, *Combust. & Flame* **80**, 264–279 (1990).

31. V. H. Ransom, Numerical benchmark tests, in *Multiphase Science and Technology*, edited by Hewitt, Delhaye and Zuber (Hemisphere, Washington, DC, 1987), Vol. 3.

32. X. Rogue, *Expériences et simulations d'écoulements diphasiques en tube à choc*, Thèse de doctorat, Université de Provence (1997).

33. X. Rogue, G. Rodriguez, J. F. Haas, and R. Saurel, Experimental and numerical investigation of the shock-induced fluidization of a particle bed, *Shock Waves* **8**, 29–45 (1998).

34. V. V. Rusanov, Calculation of interaction of non-steady shock waves with obstacles, *J. Comput. Math. & Phys. USSR* **1**, 267–279 (1961).

35. L. Sainsaulieu, Finite volume approximations of two phase fluid flows based on an approximate Roe-type Riemann solver, *J. Comput. Phys.* **121**, 1–28 (1995).

36. R. Saurel, M. Larini, and J. C. Loraud, Ignition and growth of a detonation by a high energy plasma, *Shock Waves* **2**, No. 1, 91–102 (1992).

37. R. Saurel, E. Daniel, and J. C. Loraud, Two-phase flows: Second order scheme and boundary conditions, *AIAA J.* **32**, No. 6, 1214–1221 (1994).

38. R. Saurel, M. Larini, and J. C. Loraud, Exact and approximate Riemann solver for real gases, *J. Comput. Phys.* **112**, No. 1, 126–137 (1994).

39. R. Saurel, Numerical analysis of Ram Accelerator employing two-phase combustion, *AIAA J. Propulsion & Power* **12**, No. 4, 708–717 (1996).

40. R. Saurel and R. Abgrall, A simple method for compressible multifluid flows. *SIAM J. Sci. Comput.*, in press.

41. R. Saurel and J. Massoni, On Riemann problem based methods for detonation in solid energetic materials, *Int. J. on Numer. Methods in Fluids* **26**, 101–121 (1998).

42. R. Saurel and T. Gallouet, Modèles et méthodes numériques pour les écoulements fluides, Cours de DEA , Centre de Mathématiques et d'Informatique, Université de Provence (1998).

43. R. Saurel, J. P. Cocchi, and P. B. Butler, A numerical study of the cavitation effects in the wake of a hypervelocity underwater projectile, *AIAA J. Propulsion & Power*, in press.

44. K. M. Shyue, An efficient shock-capturing algorithm for compressible multicomponent problems, *J. Comput. Phys.* **142**, 208 (1998).

45. Strang, On the construction and comparison of difference schemes. *SIAM J. Numer. Anal.* **5**, No 3, 506–517 (1968).

46. E. F. Toro, Riemann-problem based techniques for computing reactive two-phase flows, in *Proceedings, Third International Conference on Numerical Combustion, Antibes, France, May 1989*, edited by Dervieux

and Larrouturrou, Lecture Notes in Physics (Springer-Verlag, New York/Berlin, 1989), Vol. 351, pp. 472–481.

47. E. F. Toro, Some IVPs for which conservative methods fail miserably, in *Proceedings, 6th International Symposium on Computational Fluid Dynamics, Lake Tahoe, California, September 4–8, 1995.*

48. E. F. Toro, *Riemann Solvers and Numerical Methods for Fluid Dynamics* (Springer-Verlag, Berlin, 1997).

49. I. Toumi and A. Kumbaro, An approximate linearized Riemann solver for a two-fluid model, *J. Comput. Phys.* **124**, 286–300 (1996).

50. B. van Leer, Toward the ultimate conservative difference scheme. V. A second order sequel to Godunov's method, *J. Comput. Phys.* **32**, 101 (1979).